


Article

A Study on the Influence of Nonlinear Vibration on Fretting Damage of Involute Spline Pairs in Aero-Engines

Xiangzhen Xue ^{1,*}, Yifan Li ¹ , Kuan Lin ¹, Liqi Sui ², Yiqiang Jiang ³ and Ning Zhang ¹

¹ College of Mechanical and Electrical Engineering, Shaanxi University of Science and Technology, Xi'an 710021, China; 210512100@sust.edu.cn (Y.L.); 220512094@sust.edu.cn (K.L.); 220511005@sust.edu.cn (N.Z.)

² Yibin Fengchuan Powertrain Technology Co., Ltd., Yibin 644002, China; suiliqi@126.com

³ Department of International Applied Technology, Yinbin University, No.8. Luke, Wuliangye Avenue, Yibin 644000, China; 210512055@sust.edu.cn

* Correspondence: xuexiangzhen@sust.edu.cn

Abstract: To meticulously examine the repercussions of nonlinear vibrations on fretting damage within aero-engine involute spline pairs, a dynamic model was constructed rooted in well-established theories and methodologies. MATLAB was engaged to resolve the model, where the vibration displacement function was treated under Fourier transformation. The emergent sub-model was then integrated into finite element analysis software to scrutinize the distribution curves of fretting damage over the external spline tooth surface. The analysis included a comprehensive comparison of the axial and radial distributions, in addition to scenarios with and without vibration interferences. Further, an empirical platform was devised to authenticate the outcomes harvested through finite element simulation. The results indicate that the principal mode of fretting damage failure in aero-engine involute spline pairs fundamentally comprises fretting wear. This wear occurs throughout the rotational period of the fretting cycle and reciprocally interacts with fretting fatigue phenomena. Significantly, it was ascertained that acute nonlinear vibrations escalate the magnitude of fretting damage and the quantity of worn teeth within aero-engine spline pairs. Beyond that, angular misalignment was recognized as an aggravating factor that compounds fretting damage in the secondary bond teeth of involute spline pairs. These newfound insights are of paramount significance for the strategic design of involute splines to combat wear.



Citation: Xue, X.; Li, Y.; Lin, K.; Sui, L.; Jiang, Y.; Zhang, N. A Study on the Influence of Nonlinear Vibration on Fretting Damage of Involute Spline Pairs in Aero-Engines. *Lubricants* **2023**, *11*, 515. <https://doi.org/10.3390/lubricants11120515>

Received: 23 September 2023

Revised: 15 November 2023

Accepted: 24 November 2023

Published: 6 December 2023



Copyright: © 2023 by the authors. Licensee MDPI, Basel, Switzerland. This article is an open access article distributed under the terms and conditions of the Creative Commons Attribution (CC BY) license (<https://creativecommons.org/licenses/by/4.0/>).

Keywords: mechanical engineering; involute spline; finite element; fretting damage; nonlinear vibration; anti-attribution

1. Introduction

In accord with prevalent statistics, rotor vibration occurrences contribute to approximately 80% of mechanical mishaps that occur during rotation processes. The resulting fallouts encompass fatigue, fractures, and additional malfunctions in, but not limited to, shafting components. Consequently, these failings precipitate substantial safety abnormalities [1]. Consequently, an abundance of academic studies have pursued the vibrational traits of spline rotor systems in recent years. For instance, scholarly work carried out by Huang, Z.L. et al. [2] acknowledged the nonlinear elements of spline meshing gaps and rolling bearing contact. Their research generated a nonlinear dynamic model of a rotor-bearing system exhibiting the properties of both flexural and torsional coupling. This breakthrough model now offers simplified ways to mitigate vibration and to design dynamically efficient rotor-bearing systems [2]. In a separate study, Long, X. et al. [3] embarked on the analysis of the impacts inflicted on the internal spline's unusual wear due to determinants such as tooth surface hardness, vibration, and rotation precision. This exploration, which was premised on the features of involute spline connections, provides pivotal information for the conceptualization of accessory actuators [3]. Zeng, G. et al. [4]

devised a coupling vibrational dynamics model for rotor–planetary gearing systems within the scope of the electromechanical compound transmission. Their research elucidated the vibration characteristics of the rotor–planetary gear system at various velocities. It extrapolated insights concerning the coupling vibration interaction between the gear system and the rotor of the propulsion motor. These enlightenments establish a theoretical scaffold for the expedited design of transmission systems [4]. Du, W.L. et al. [5] successfully derived the coupling dynamic equation applicable to a rotor system subjected to load excitation, utilizing the formidable computational prowess of Lagrange’s equation. The team conducted an array of numerical simulations reliant upon the Runge–Kutta computation methodology, permitting them to scrutinize the coupling vibration properties intrinsic to the motor rotor system under an assortment of load excitations. This seminal work yielded pivotal insights to inform and refine active vibration reduction stratagems pertinent to rotor systems [5]. Wang, P.F. et al. [6] embarked on a critical exploration centering on the repercussions of misalignment upon the dynamic contact attributes of bearings in addition to the vibration characteristics inherent in rotor systems. Pivotal among their findings is the revelation that bearing misalignment exponentially accelerates the resonance speed of the rotor while concurrently triggering amplitude hopping within the resonance domain. These seminal revelations provide a sturdy theoretical foundation as well as an invaluable cache of references for routine and advanced fault-identification tasks within rotor-bearing systems [6]. Under the expert guidance of Wang, L.K. et al. [7], dynamic models of intricate rotor-support systems, such as those found in aero-engines, were conceptualized. Experiments were thereafter conducted to authenticate the efficacy of these carefully constructed models. The team further dissected the nonlinear damping efficiency of parallel extruding oil film dampers (SFDs) in conjunction with elastic supports. Their research is a trove of quantitative references critical to the parallel design of aero-engine support stiffness and correlating SFDs [7]. Ge, W.W. [8] and his team established a comprehensive rotor-bearing system and pragmatically relied on the Runge–Kutta method for integral computations. The research team’s investigation hinged upon the discernible influences of support stiffness, damping, acceleration, and support position on rotor vibration traits [8].

Scholars have conducted extensive investigations into the vibration characteristics of rotors featuring misaligned spline couplings. Xiao, L. et al. meticulously devised a nonlinear dynamic model tailored to misaligned spline couplings and scrutinized the dynamic meshing behavior exhibited by misaligned tooth pairs [9]. Mura, A. et al. employed finite element analysis to delve into the ramifications of eccentricity angle and transfer torque, culminating in a theoretical model addressing inclination torque [10–12]. Guo, Y. et al. put forth an innovative model to analyze gear couplings, taking into account variables such as load torque, misalignment, and friction [13]. Zhao, G. et al. conducted simulations, unearthing the consequences of misaligned meshing force upon the dynamics of rotor–spline coupling systems, and subsequently derived a differential equation pertinent to the dynamics of toothed couplings [14–16]. He, C.B. meticulously examined the misalignment concerns intrinsic to tooth couplings and their corresponding rotor systems [17]. Fu, B. delved into the impact of parallel misalignment on fixed rigid couplings [18]. Jing, J.P. and Gao, T. [19,20] computed the dynamic load coefficient emblematic of a secondary spline system, established a vibration model predicated on the finite element method, and analyzed the effects of dynamic engagement forces on the rotating subsystem’s stability. Through rigorous theoretical analysis and experimental research, they unveiled the influence of various dynamic parameters on the system’s characteristics and stability [19,20]. Furthermore, researchers have probed the effects of misalignment on the vibration characteristics intrinsic to spline coupling systems [21–23].

The interpretation and analysis of load dispersion and spline principles have been acknowledged critical for the prognosis of fretting deterioration in spline couplings. Such matters have been earnestly explored by experts [24–26]. Subsequently, Xue, X.Z. formulated a solely torsional dynamic model as well as a dynamic equation for involute spline combinations localized in aero-engines. They proceeded to compute the all-encompassing

mesh rigidity, further assess the dynamic payload, and scrutinize the vibration displacement intrinsic to the spline coupling assembly [27–29]. Surprisingly, it was found that the pragmatic logarithm of meshing teeth within involute spline combinations diverged from the theoretical estimation and varied in accordance with external payloads and lateral tooth flexibility, precipitating a temporal variation in meshing rigidity. In addition to this, installation-induced or operation-induced (originating from heat, payload, foundational deformation, etc.) misalignment of internal and external spline shafts, as well as manufacturing discrepancies resulting in mass eccentricity and tooth flexibility, engender bending and superior payloads on the spline shafts. This scenario culminates in the creation of nonlinear, flexural–torsional, amalgamated oscillations within the involute spline sub-categories. At the present moment, the majority of the research work pertaining to spline couplings is majorly concentrated on the coupling itself—ironically overlooking the reality that spline constructions are not solely employed within shaft couplings but also find widespread applications in various other transmission domains. Hence, the prevalence of studies evaluating vibration and its subsequent influence on fretting damage within this scenario is alarmingly scarce.

Thus, this investigation primarily pivots its attention towards precisely determining the dynamic parameters attributable to the secondary structure within involute spline pairs utilized in aero-engines. Subsequently, these findings are integrated with the execution of finite element simulation, which vigorously enables the analysis of various vibro-characteristics' impact on fretting damage in involute spline pairs. Additionally, this study comprehensively examines how angulated misalignment influences nonlinear vibrations as well as fretting damage. The insights gleaned from this research hold instrumental value for the blueprinting of high-performance, reliable, and resilient involute spline pairs specifically tailored for utilization within aero-engines. Furthermore, aero-engine involute spline pairs inherently exhibit complex, nonlinear dynamic characteristics through the manifestation of transverse, torsional, and longitudinal vibrations within the scope of the rotor system. These vibrations, unfortunately, are potent enough to inflict destructive ramifications on the integrity both of spline pairs and the associated shafting [30]. Misalignment aberrations represent a conventional fault within spline and rotor system frameworks. In instances where misaligned configurations morph into the predominant source of faults, one can expect detrimental outcomes such as pronounced structural damage to the spline mechanism, exacerbated system vibrations, and the emergence of substantial safety-related implications. Last but not least, the intricacies of the operational process tied to aero-engine involute spline pairs inevitably instigate micro-amplitude vibrations within the secondary system framework. These vibrations precipitate substantial fretting damage, drastically curtailing the operational lifespan of the implicated components [31,32].

In a concerted effort to efficaciously modulate the vibration and attenuate fretting wear associated with aero-engine involute spline couplings, the authors originated a bending–torsion unified nonlinear vibration model. This model was specifically constructed for involute spline couplings experiencing instances of misalignment. In tandem, a dynamic meshing stiffness function accommodating multi-tooth engagement was duly formulated [33]. Nevertheless, reference [33] did not account for the ramifications of spline vibration specifically on the extent of fretting damage, thereby leaving a gap in the study. Therefore, standing as a progression from the preceding investigation, this study delves into the mechanism underlying vibration-induced displacement, and extemporaneously investigates the influence of various contributory factors on fretting damage. These investigations specifically pertain to splines functioning under diversely angled misalignment conditions. A comprehensive depiction of the process is presented in Figure 1.

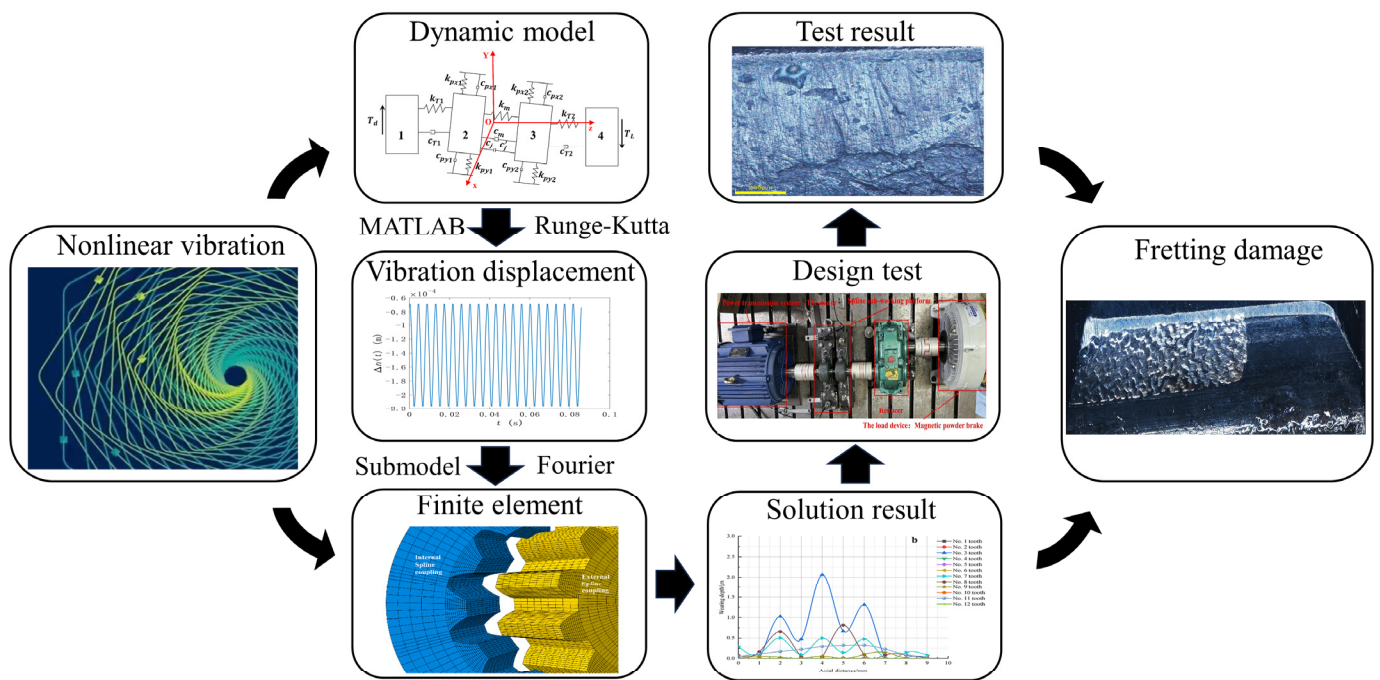


Figure 1. Flow diagram.

2. Nonlinear Dynamics Model and Solution of Involute Spline Pairs of Aero-Engine

Taking into account the aforementioned variables, this present research meticulously structures the dynamic model and dynamic differential equation for aero-engine involute spline pairs, incorporating considerations of misalignment, transverse, and torsional vibrations. By diligently resolving these equations, we ascertain the flux patterns of vibration displacement and vibration frequency, alongside other parameters under diverse conditions of angular misalignments. The comprehension of these findings provides an indispensable empirical reference for future investigations, particularly those seeking to understand the overall consequence of vibration on fretting damage in ensuing studies.

2.1. Dynamic Equation and Parameters

In this work, the centralized mass method is adopted to establish a three-dimensional dynamics model for the involute spline pairs of an aero-engine system [33], as shown in Figure 2.

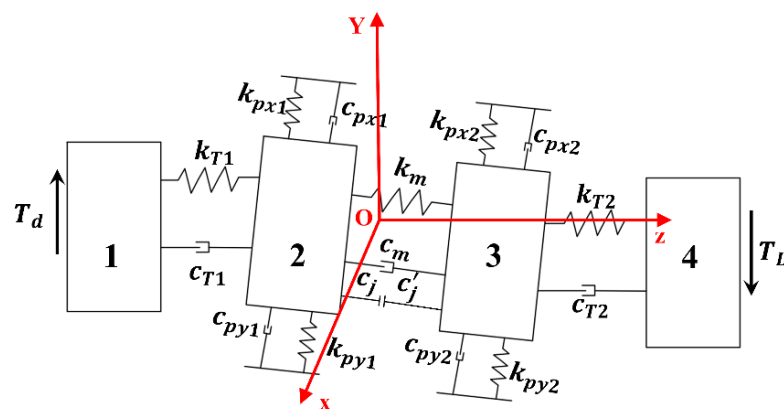


Figure 2. Dynamics model of involute spline pairs of aero-engine secondary system (1—electromotor; 2—external spline; 3—internal spline; 4—load device).

Newton’s second law is adopted to establish the differential equation of involute spline pairs of aero-engine secondary dynamics [30–32]. Assuming that the internal and

external spline support stiffness and support damping are the same in x and y directions, the dynamic equation [33] is as follows:

$$\left\{ \begin{array}{l} J_M \ddot{\theta}_M + k_{T1}(\theta_M - \theta_1) + c_{T1}(\dot{\theta}_M - \dot{\theta}_1) = T_d \\ m_1 \ddot{x}_1 + k_{p1}x_1 + c_{p1}\dot{x}_1 = F_{mx} \\ m_1 \ddot{y}_1 + k_{p1}y_1 + c_{p1}\dot{y}_1 = F_{my} - m_1g \\ J_1 \ddot{\theta}_1 + k_{T1}(\theta_1 - \theta_M) + c_{T1}(\dot{\theta}_1 - \dot{\theta}_M) = T_m \\ m_2 \ddot{x}'_2 + k_{p2}x'_2 + c_{p2}\dot{x}'_2 = -F_{mx} \\ m_2 \ddot{y}'_2 + k_{p2}y'_2 + c_{p2}\dot{y}'_2 = -F_{my} - m_2g \\ J_2 \ddot{\theta}_2 + k_{T2}(\theta_2 - \theta_L) + c_{T2}(\dot{\theta}_2 - \dot{\theta}_L) = -T_m \\ J_L \ddot{\theta}_L + k_{T2}(\theta_L - \theta_2) + c_{T2}(\dot{\theta}_L - \dot{\theta}_2) = -T_L \end{array} \right. \quad (1)$$

in which J_M is the moment of inertia of the motor ($\text{kg}\cdot\text{m}^2$); J_u is the moment of inertia of the involute spline pairs ($\text{kg}\cdot\text{m}^2$); m_u is the mass of involute spline pairs (kg); k_{T1} is the torsional stiffness between the motor and the external spline ($\text{N}\cdot\text{m}/\text{rad}$); c_{T1} is the torsional stiffness between the motor and the internal spline ($\text{N}\cdot\text{m}\cdot\text{s}/\text{rad}$); k_{T2} is the torsional stiffness between the internal spline and the load ($\text{N}\cdot\text{m}/\text{rad}$); c_{T2} is the torsional damping between the internal spline and the load ($\text{N}\cdot\text{m}\cdot\text{s}/\text{rad}$); k_{pu} is the support stiffness at the spline (N/m); c_{pu} is the support damping at the spline ($\text{N}\cdot\text{s}/\text{m}$); x'_2 is the x-direction vibration displacement of the internal spline in consideration of parallel misalignment ($x'_2 = x_2 + l_x$, l_x is the x-direction misalignment (m)); y'_2 is the y-direction vibration displacement of the internal spline considering parallel misalignment ($y'_2 = y_2 + l_y$, l_y is the y-direction misalignment (m)); F_{mx} is the x-direction component of the meshing force of the external spline (N); F_{my} is the y-direction component of the meshing force of the external spline (N); T_m is the meshing torque and torque at the external spline ($\text{N}\cdot\text{m}$); T_d is the system input torque ($\text{N}\cdot\text{m}$); T_L is the load torque ($\text{N}\cdot\text{m}$); $u = 1, 2$ (1 is the external spline, 2 is the internal spline). Since torsional degrees of freedom are unconstrained in all degrees of freedom, rigid body displacement around the z axis of the spline will occur, and the result cannot be convergent. In order to eliminate this rigid body displacement, dimensionless treatment is carried out on the differential equations, and the dimensionless reference parameter ω, l is introduced to estimate the value of the first natural frequency of the system according to the Rayleigh method, whose dimensionless reference parameter $\omega = 1.3409 \times 10^3$ Hz [33]; l takes the value c_0 of the spline side forward backlash.

The relative displacement formula of spline meshing line is [33]:

$$\Delta n_j(t) = (x_1 - x'_2)\sin \varphi_j - (y_1 - y'_2)\cos \varphi_j + r_b(\theta_2 - \theta_1) \quad (2)$$

The angle between the flank line of tooth profile and x direction φ_j is [33]:

$$\varphi_j = \theta_j - \alpha_0 = 2\pi j/z + \omega_0 t + \theta_0 - \alpha_0 \quad (3)$$

in which θ_0 is half angle of tooth thickness of dividing round tooth; ω_0 is the spline angular velocity (rad/s); α_0 is the pressure angle; z is the number of teeth.

Due to the transverse vibration and misalignment, the position of the meshing point of the key teeth changes with the vibration and misalignment, leading to the change of the load position of the key teeth, and the meshing stiffness changes accordingly. Therefore, the dynamic position of the meshing point on the key tooth is calculated by taking the vibration displacement as the initial condition. The displacement of the meshing point moving along the tooth profile is [33]:

$$l_{ED} = \Delta_y \sin \theta_i + \Delta_x \cos \theta_i \quad (4)$$

Due to the transverse vibration and misalignment, the position of the meshing point will change, so that the meshing angle, the height of the micro tooth segment, and the surface half-tooth thickness of the micro tooth segment will be different, and the stiffness will also change. In this work, the involute spline pairs of the aero-engine are meshed laterally, so only tangential stiffness is considered, and the basic deformation of shaft and yield compression deformation are ignored. The total meshing stiffness of the first pair of teeth is [33]:

$$\left\{ \begin{array}{l} \Delta_{b,u} = \frac{1}{E_\mu} \left[\frac{\cos^2 \varphi}{3} \sum_{v=1}^n \frac{h_u}{I_{v,u}} (h_u^2 + 3S_{v,u}h_u + 3S_{v,u}^2) \right. \\ \left. - Y_F \cos \varphi \sin \varphi \sum_{v=1}^n \frac{h_u}{I_{v,u}} (h_u + 2S_{v,u}) + Y_F^2 \sin^2 \varphi \sum_{v=1}^n \frac{h_u}{I_{v,u}} \right] \\ \Delta_{s,u} = \frac{1.2 \cos^2 \varphi}{G} \sum_{v=1}^n \frac{h_u}{A_{v,u}} \\ \Delta_T = \Delta_{b,1} + \Delta_{b,2} + \Delta_{s,1} + \Delta_{s,2} \\ K_m = K_T = \frac{1}{\Delta_T} \end{array} \right. \quad (5)$$

in which $\Delta_{b,u}$ is the flexural flexibility ($u = 1, 2$; 1—external spline; 2—internal spline); E_μ is the elasticity modulus; φ is the contact angle of the engagement point (rad); h_u is the height of the loaded micro end of the key tooth; $I_{v,u}$ is the moment of inertia of the v tooth section; $S_{v,u}$ is the distance between the spline pitch circle and the surface of the v tooth segment; Y_F is half tooth thickness of the dividing circle ($Y_F = 0.25 \pi m$) [33]; $\Delta_{s,u}$ is shear flexibility; G is the shear modulus; $A_{v,u}$ is the average surface area of the upper and lower surfaces of the v tooth segment; Δ_T is the total flexibility of the tooth; K_m is the total meshing stiffness of the teeth (N/m).

The formula of the total meshing force of each tooth of the external spline and the component force along the coordinate axis is [33]:

$$\left\{ \begin{array}{l} F_{nj} = k_m g_j [\Delta n_j(t)] + c_m \dot{g}_j [\Delta n_j(t)] \\ F_{mx} = -\sum_{j=1}^z F_{nj} \sin \varphi_j \\ F_{my} = \sum_{j=1}^z F_{nj} \cos \varphi_j \end{array} \right. \quad (6)$$

in which F_{nj} is the total meshing force of a single tooth along the meshing line; $g_j[\Delta n_j(t)]$ is the function of mesh deformation of a single pair of teeth; $\dot{g}_j[\Delta n_j(t)]$ is the single tooth meshing deformation function-derived function; k_m is the total meshing stiffness of the teeth (N/m); c_m is the meshing damping of a single pair of teeth (N·s/m).

In this experiment, the shaft between the external spline and the motor and the internal spline and the load is a step shaft with a variable section. For convenience of calculation, the torsional stiffness of shafting is calculated as follows [33]:

$$k_T = \frac{\pi G D_{min}^4}{32 L_d} \quad (7)$$

in which G is the shear elastic modulus of the material (p_a), taken as 80 Gp_a [33]; D_{min} is the minimum section diameter of the shaft (m); L_d is equivalent length of step axis (m), $L_d = \sum_{k=1}^n L_k \frac{D_{min}^4}{D_k^4}$, L_k is length of each step shaft (m), D_k is diameter of each step shaft (m), k is number of steps. According to the torsion formula, the stiffness calculation formula can be calculated as follows: torsional stiffness of external spline $k_{T1} = 7.856 \times 10^4 \text{ N}\cdot\text{m}/\text{rad}$ [33]; torsional stiffness of internal spline $k_{T2} = 7.751 \times 10^4 \text{ N}\cdot\text{m}/\text{rad}$ [33].

The formula for calculating meshing damping is as follows [33]:

$$c_m = 2\zeta_m \sqrt{k_m \frac{r_b^2 J_1 J_2}{J_1 + J_2}} \quad (8)$$

in which ξ_m is the meshing damping ratio. The value ranges from 0.03 to 0.17; in this work, the value is 0.1 [33].

The formula for calculating torsional damping is as follows [33]:

$$\begin{cases} c_{T1} = 2\xi_T \sqrt{k_{T1} \frac{J_M J_1}{J_M + J_1}} \\ c_{T2} = 2\xi_T \sqrt{k_{T2} \frac{J_L J_2}{J_L + J_2}} \end{cases} \quad (9)$$

in which ξ_T is the torsional damping ratio of material. The value ranges from 0.005 to 0.075; in this work, the value is 0.007 [33].

2.2. Solution of Dynamic Equation

In order to obtain a solution that satisfies the accuracy of the differential equation, the Runge–Kutta method is adopted in this work. The fourth-order Runge–Kutta method iteration formula is as follows:

$$\begin{cases} y_{i+1} = y_i + \frac{h}{6}(k_1 + 2k_2 + 2k_3 + k_4) \\ k_1 = f(t_i, y_i) \\ k_2 = f(t_i + \frac{h}{2}, y_i + \frac{hk_1}{2}) \\ k_3 = f(t_i + \frac{h}{2}, y_i + \frac{hk_2}{2}) \\ k_4 = f(t_i + h, y_i + hk_3) \end{cases} \quad (10)$$

In this work, MATLAB was adopted to solve the problem, and the solving command was ode45 [33], the Runge–Kutta method based on variable step size. Before solving the dynamic equation, it was necessary to reduce the order of the dynamic differential equation to eliminate the rigid body displacement and dimensionless. Therefore, new variables have been introduced to replace and process the higher-order terms in the differential equation, and the higher-order terms of the differential equations are constantly replaced until the higher-order terms of the differential equations are replaced by the first-order ordinary differential equations. In order to replace the degree of freedom of differential equation, a new set of state variables $q_1 \sim q_{14}$ is introduced, corresponding to the differential equation $\{\bar{x}_1, \dot{\bar{x}}_1, \bar{y}_1, \dot{\bar{y}}_1, \bar{x}_2, \dot{\bar{x}}_2, \bar{y}_2, \dot{\bar{y}}_2, \bar{\Delta}_1, \dot{\bar{\Delta}}_1, \bar{\Delta}_2, \dot{\bar{\Delta}}_2, \bar{\Delta}_3, \dot{\bar{\Delta}}_3\}$. After the above treatment, the ode45 function can be used to solve the equation iteratively. The initial value of the iteration parameter q is taken as an all-zero vector. The parameters required to solve the dynamic differential equation in this work are shown in Table 1:

Table 1. Parameter values of differential equation [33].

Parameter	Parameter Value	Units
J_M	7.54×10^{-3}	kg·m ²
J_L	7.5263×10^{-3}	kg·m ²
J_1	3.4358×10^{-3}	kg·m ²
J_2	3.7321×10^{-3}	kg·m ²
m_1	4.5106	kg
m_2	4.5572	kg
k_{p1}, k_{p2}	5×10^6	N/m
c_{p1}, c_{p2}	5	N·s/m

Single side clearance $c_0 = 7.95 \times 10^{-5}$ m [33]; load torque $T_L = 28$ N·m [33]; according to the energy dissipation relation, driving moment $T_d = 30.67$ N·m [33]; input speed $n = 1400$ r/min. The solution results are shown in Figures 2–4 in Section 2.

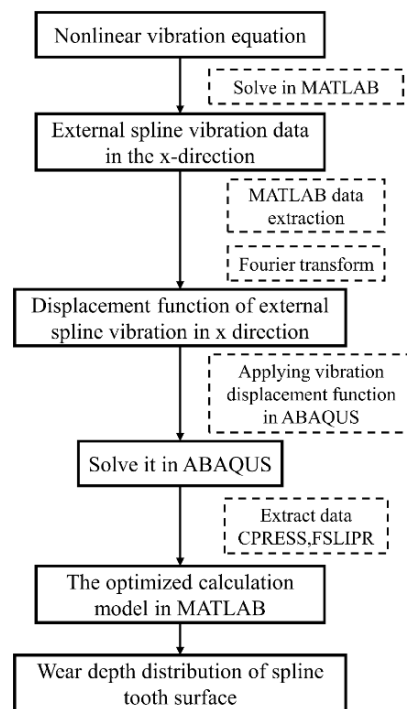


Figure 3. Flow chart of calculating fretting damage of involute spline pairs of an aero-engine under the influence of nonlinear vibration.

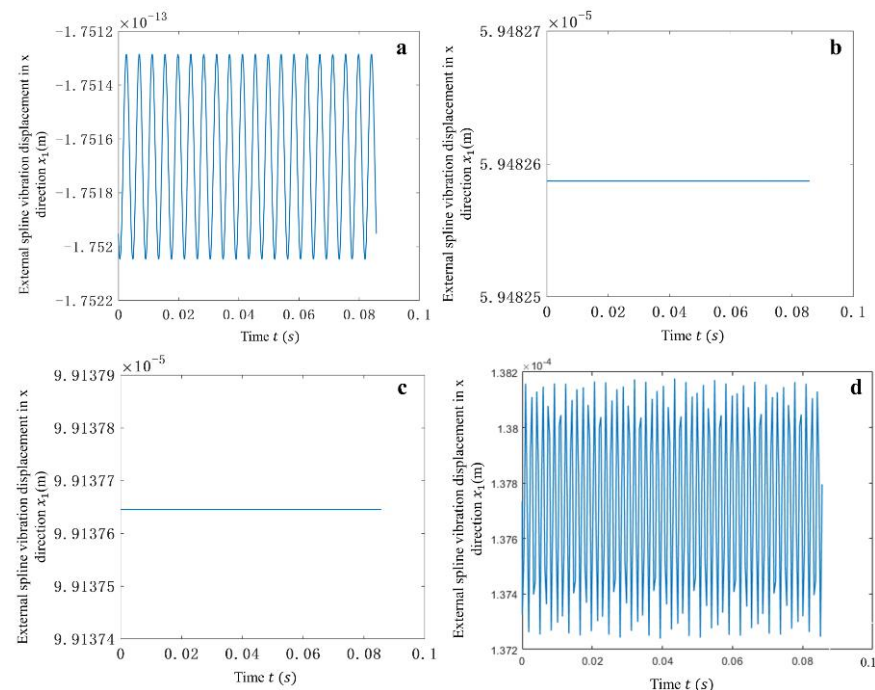


Figure 4. Vibration displacement curve of external spline in x direction: (a) $e = 0^\circ$ (b) $e = 0.1^\circ$ (c) $e = 0.2^\circ$ (d) $e = 0.3^\circ$.

3. Fretting Damage Prediction Model for Involute Spline Pairs of an Aero-Engine

Upon a careful investigation, existing studies [34] have attested to the fact that although fretting fatigue pervades throughout the entire fretting cycle and exhibits competition and influence alongside fretting wear, the predominant manifestation of fretting damage failure within the involute spline pairs of an aerodynamic engine is ultimately and specifically characterized by the fretting wear failure mechanism. Thus, with a focus

on highlighting the intricate interrelations between the observed phenomena, this current work opts to use the wear depth of the spline as a reference point. The aim here is to illuminate the underlying mechanisms through which nonlinear vibrations exert a potential impact on the ensuing fretting damage.

Based on the Archard abrasive wear and adhesive wear model, the fretting wear model suitable for involute spline pairs of an aero-engine was derived. In the abrasive wear model, i.e., the wear volume obtained by the normal load on a solid abrasive particle (Equation (11)), the wear volume obtained after the abrasive particle is pressed into the depth Z of the ground surface and slides δ_L distance on the surface (Equation (12)), and the total wear rate of the abrasive particle under unit slip distance is obtained by dividing both ends of Equation (2) by the slip distance δ_L (Equation (13)):

$$\delta_N = \frac{\pi}{2} B^2 H \quad (11)$$

$$\delta_V = \frac{2\delta_N \delta_L}{\pi t g_\theta H} \quad (12)$$

$$R_V = K \frac{N}{H} \quad (13)$$

in which δ_N is the normal load borne by the abrasive particles (Mpa); H is hardness; δ_V is the abrasive wear volume (mm^3); δ_L is the abrasive slip distance; R_V is the total wear rate of abrasive particles; K is abrasive wear coefficient.

For adhesive wear, the microscopic cutting theory is also adopted. Different from abrasive wear, which assumes abrasive particles as cones, and adhesive wear, which assumes abrasive particles as spheres, the Archard adhesive wear model is obtained, as shown in Equation (14) [29]:

$$R_V = k_n \frac{N}{3\sigma} \quad (14)$$

in which R_V is the adhesive wear volume (mm^3); k_n is the adhesion wear coefficient; N is the normal load borne by the abrasive particle (Mpa); σ is the yield stress (Mpa).

For the calculation of fretting wear, domestic and foreign scholars have derived the Archard calculation model suitable for fretting wear by combining the above abrasive wear model and adhesive wear model, as shown in Equation (15):

$$h = 2k \cdot s \cdot p \quad (15)$$

in which h is the wear depth (mm); k is the wear coefficient; s is the relative slip distance (mm); p is the contact stress (Mpa). However, in order to make the above formula more suitable for the special working condition of involute spline pairs of an aero-engine, the above formula is optimized as follows.

As the contact stress on the surface of spline teeth of involute spline pairs of an aero-engine is constantly changing during the working process, and the relative slip rate between spline couplings is also constantly changing within a certain period of time, the above equation is differentiated and integrated on both sides to obtain the optimized Archard calculation model, as shown in Equation (16):

$$h_j = 2K \int_{t_1}^{t_2} (v_{0j} \cdot p) dt \quad (16)$$

in which $v_{0j}(t)$ is the velocity change curve at a node of the spline tooth surface (mm/s); $p(t)$ is the stress change curve at a node of the spline tooth surface (Mpa).

The methodology for discerning fretting damage experienced by secondary involute spline pairs in aero-engines under the exertion of nonlinear vibrations follows these outlined steps:

1. Solving the differential equation specified in Section 1 utilizing MATLAB results in the derivation of the external spline's vibration displacement curve, specifically oriented in the x -axis direction.
2. Data relevant to the external spline's vibration displacement in the x -axis direction are gleaned and solved through Fourier transform within MATLAB to yield a time-based function. This function delineates the vibrational displacement's variability.
3. The resultant function is applied to the displacement boundary condition of the spline in the x direction using ABAQUS, an advanced computational platform, and ensuingly resolved.
4. Post resolution within ABAQUS, the CPRESS and rate FSLIPR in the resultant data file are scrutinized. Subsequently, MATLAB is employed to optimize the Archard fretting wear calculation model, facilitating the estimate of the wear depth distribution on the external spline's tooth surface in conjunction with different vibrational displacements. A more explicit illustration of this calculation process is demonstrated in Figure 3.

4. Analysis of Nonlinear Vibration Characteristics of Involute Spline Pairs of an Aero-Engine

4.1. Study on the Influence of Different Angle Misalignment on Vibration Displacement of Involute Spline Pairs

As illustrated in Figure 4a, each pair of interlocking teeth generates a corresponding meshing force upon exposure to exerted loadings. The key teeth, distributed uniformly around the circumference, induce forces that correspond to their respective X -component forces within designated quadrants. In situations where the tooth count is even and the side clearance remains unvaryingly uniform for all tooth pairings, any assumptions disregarding angular misalignment ultimately culminate in the neutralization of X -directional component forces spanning the entirety of the key teeth. As a consequence, the external spline's vibrational displacement along the x axis is notably diminished, registering an approximate order of magnitude of 10^{-13} . This value, being nearly negligible, suggests that the spline experiences minimal vibrational activity along the x axis. In Figure 4b, it is observed that the external spline's x -directional vibrational displacement begins to amplify noticeably, operating within an order of magnitude of 10^{-5} . Despite its displacement curve nearly adopting a linear guise, it still expresses periodic characteristics when the magnitude approaches an order of 10^{-13} . Likewise, as shown in Figure 4c, the external spline's x -directional vibrational displacement persists in its rising trajectory while maintaining an order of magnitude of 10^{-5} . By the time we reach Figure 4d, the same x -directional displacement of the external spline elevates further to reach an order of magnitude of 10^{-4} . These observations postulate that the vibrational displacement for involute spline pairs will escalate in correlation with growing angular misalignment. It is noteworthy that angular misalignment presents its most dramatic rise between 0 and 0.1, while the increment between 0.1 and 0.3 proves substantially less pronounced.

4.2. Study on the Influence of Different Angle Misalignment on Vibration Frequency of Involute Spline Pairs

In Figure 5a, no appreciable displacement amplitude can be discerned across the 0–2000 Hz frequency band, which intimates that the vibration-induced dynamic stress remains inconsequential, thus inflicting negligible damage to the system when factors of misalignment are excluded from considerations. However, in Figure 5b, there emerges a notable upward surge in displacement amplitude proximate to the 250 Hz mark, scaling to an estimated value of 0.25 m, and an order of magnitude of 10^{-4} . Contrasted against the dynamic stress resultant from vibrational phenomena in the fully aligned scenario, this increment signals an escalation in the potential detrimental influences on the system. Subsequently, in Figure 5c, we perceive a further growth in displacement amplitude at the 250 Hz frequency spectrum, coinciding with an increase in the vibration-induced dynamic stress and thereby potentiating system degradation. Lastly, as delineated in Figure 5d,

the aforementioned displacement amplitude at 250 Hz continues its ascent, resulting in a concomitant rise of the vibration-induced dynamic stress. Within Figure 5b–d, we observe prominent amplitude peaks within the lower frequency range. These peaks denote that the stress cycle induced by the alternating loads resultant from spline pair vibrations incessantly modulates internal stress states. As the alternating load exerts its influence, the amplitude of the dynamic stress gradually burgeons. Although the maximum stress acting within the component falls below the material's yield threshold, the fracture risk associated with key teeth incrementally magnifies upon sustained exposure to repeated loadings. Resultantly, this fracture risk becomes increasingly pronounced with higher degrees of angular misalignment, concomitantly potentiating harm to the overall system.

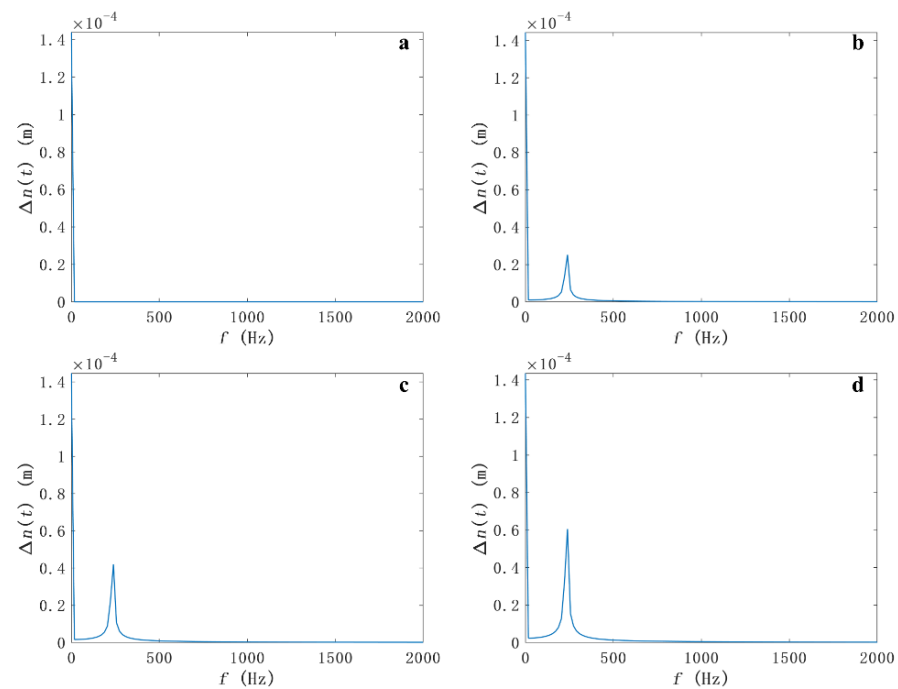


Figure 5. Variation of relative vibration displacement of external spline with frequency (a) $e = 0^\circ$, (b) $e = 0.1^\circ$, (c) $e = 0.2^\circ$, (d) $e = 0.3^\circ$.

4.3. Study on the Influence of Different Angle Misalignment on the Load of Involute Spline Pairs

As delineated in Figure 6a, the normal meshing force distribution objectified across the spline teeth exhibits a consistently uniform characteristic under conditions of uniform backlash. Encompassing teeth 1–12, this category of forces demonstrates a balanced magnitude concomitant with directional linearity towards the negative range. This implies that each tooth's inherent meshing force propagates in unison with the normal directionality of the tooth, following an inward course. Concurrently, the net torque subjected upon the external spline, as can be inferred, adheres to a negative, clockwise rotation. Transitioning to the interactional dynamics portrayed in Figure 6b, the erstwhile uniformity of regular meshing force dispersion among the external spline's teeth ceases to persist. Ubiquitously, teeth numbered 1 and 12 bear the intense brunt of the highest forces promulgated along the meshing line, while the meshing force exhibits a progressive decline for teeth enumerated sequentially from either extremity towards the midsection. Upon computational validation of the relative positioning of tooth 1, it arises that the meshing condition veers towards proximity, thereby imposing amplified loads on each tooth in direct proportionality to the misalignment magnitude of $e = 0.1^\circ$. Contrastingly, teeth discretely distant from this positioning (with specific reference to teeth 6, 7, and 8) are subjected to diminished loads. Progressing to the scenario highlighted in Figure 6c, an exacerbation in the irregularity of the normal meshing force distribution across the teeth of the external spline becomes palpable. Maintaining their precedent attributes, teeth 1 and 12 continue to endure the

peak force exerted along the meshing line, while teeth 6, 7, and 8 sustain comparatively milder loads. As we traverse from both ends towards the central region, the meshing force decrement for each tooth becomes conspicuously accentuated. Finally, as illustrated in Figure 6d, the normal meshing force acting on each tooth of the external spline amplifies in correlation with escalating misalignments. Analogous to the previous patterns, teeth already burdened with heightened loads manifest a concurrent load surge. However, an observable digression from the previous scenarios presents itself in the form of certain less-loaded teeth falling out of the meshing engagement, thereby indicating a shift in tooth compliance patterns extensive enough to disrupt the previous uniformity.

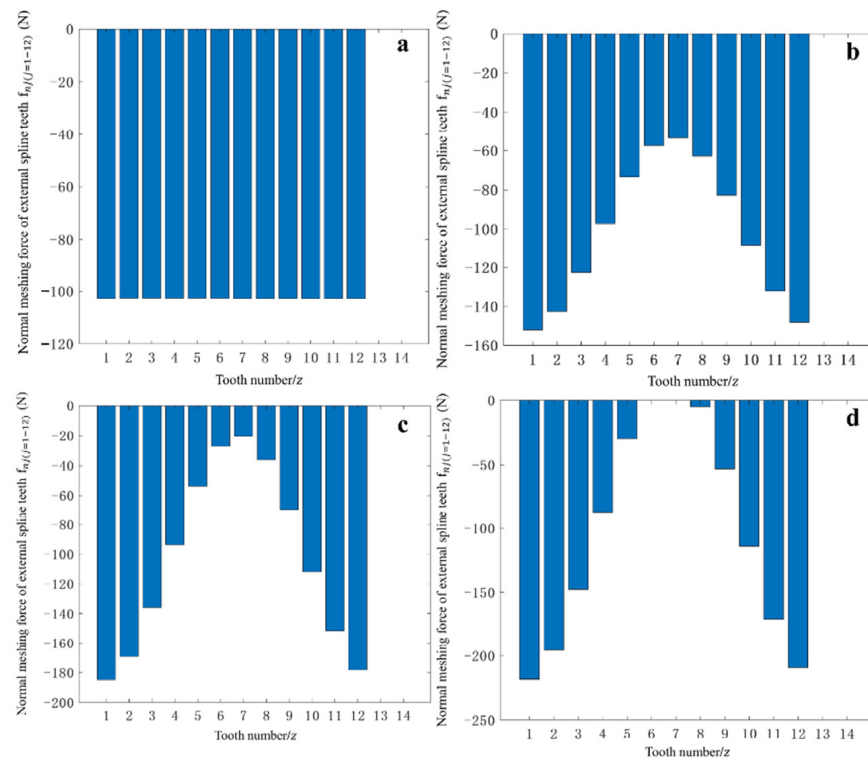


Figure 6. External spline tooth load diagram: (a) $e = 0^\circ$; (b) $e = 0.1^\circ$; (c) $e = 0.2^\circ$; (d) $e = 0.3^\circ$.

5. Analysis of the Influence of Nonlinear Vibration on Fretting Damage of Involute Spline Pairs of an Aero-Engine Based on MATLAB–ABAQUS

To conduct a simulation of the vibration of involute spline pairs using the ABAQUS software 2022, the differential equation delineated in Section 2 was initially solved through the implementation of MATLAB. Subsequently, the Fourier transform method was employed to convert the vibration displacement data pertaining to the external spline, thereby deriving the requisite displacement function. This function was then utilized as a boundary condition within ABAQUS to accurately model the vibrational behavior of involute spline pairs. Following the completion of the simulation, essential parameters such as contact stress, slip distance, and additional data were extracted from the ABAQUS outputs. To estimate the wear depth of the spline under various vibrational conditions, these parameters were further analyzed using MATLAB. The primary objective of this research centers on elucidating the influence of nonlinear vibration on fretting damage in involute spline pairs. Moreover, the findings procured in this study hold significant potential in facilitating a deeper understanding of nonlinear vibration and fretting damage in an assortment of other coupling systems.

5.1. Establishment of Finite Element Model of Involute Spline Pairs of an Aero-Engine

Within this study, the material of choice for the involute spline pairs in the aero-engine is 18CrNi4A aviation high-strength steel. This secondary material has an elastic modulus (E) de-

noted as 210 GPa and a Poisson's ratio (ν) of 0.3. The mass density (ρ) stands at 7898 kg/m³. Pertinent geometric parameters for the aero-engine's involute spline pairs are detailed in Table 2, serving as a basis for establishing the finite element depicted in Figure 7. To discern the influence of vibrational displacement on the fretting damage of involute spline pairs under varying operational conditions, the time step of this section was set at 0.1 s, mirroring the time step utilized in Section 2. For the finite element model showcased in Figure 7, a systematized meshing strategy was implemented, employing the C3D8R element type—an eight-node linear hexahedral element with linear reduction integral and hourglass control. Subsequently, the model underwent densification to bolster accuracy. The chosen contact configuration for the involute spline pairs designates the internal spline tooth surface as the master surface, while the external spline tooth surface is classified as the slave surface. The kinematic contact methodology with limited slippage was selected. Tangential and normal behaviors were set independently for contact attributes. Specifically, an isotropic penalty friction model has been utilized for tangential behavior, with a friction coefficient (μ) set at 0.2. In contrast, normal behavior engages a hard contact model. For the prescribed boundary conditions, a rotational speed of $N = 1400$ r/min is assigned to the external spline, whereas a torque of $T = 50$ N·m is imparted to the internal spline. All degrees of internal spline freedom, with the exception of rotation along the z axis, are confined. For the external spline, owing to the considerations of nonlinear vibration, rotational freedom along the z axis is sanctioned, as well as translational freedom along the x axis.

Table 2. Geometric parameters of involute spline pairs of aero-engine.

Parameter	Value
Tooth number	12
Modulus (mm)	1.25
Internal spline trunnion (mm)	25
External spline trunnion (mm)	8
Contact length (mm)	9

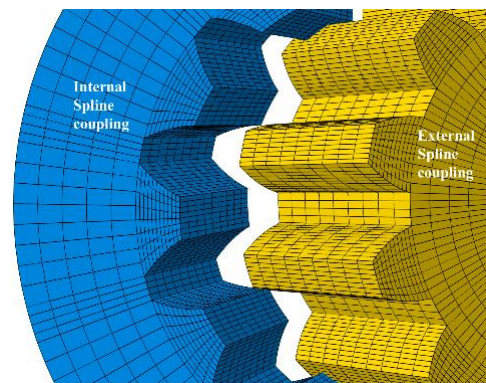


Figure 7. Finite element model of involute spline pairs of an aero-engine.

For the purpose of calibrating the finite element model, adjustments pertaining to the element size and density were executed, as explicitly delineated in Table 3. A visual representation of the stress distribution can be found in Figure 8, where Figure 8b illustrates the finite element model employed in the current study, while Figure 8a,c depict the modified versions resulting from alterations to the element parameters. The analysis reveals that fluctuations in element size and density, whether augmented or diminished, yield errors confined to a maximum of 10%. This observation substantiates the premise that the mesh maintains its independency and does not impact the ultimate computational results.

Table 3. Parameter table of the element dimensions and element density.

	Element Sizes	Element Quantity	Stress Result (Max)	Discrepancy
Figure 8a	0.5	51,264	89	8.5%
Figure 8b	0.5625	42,480	82	/
Figure 8c	0.6429	36,580	70	9.7%

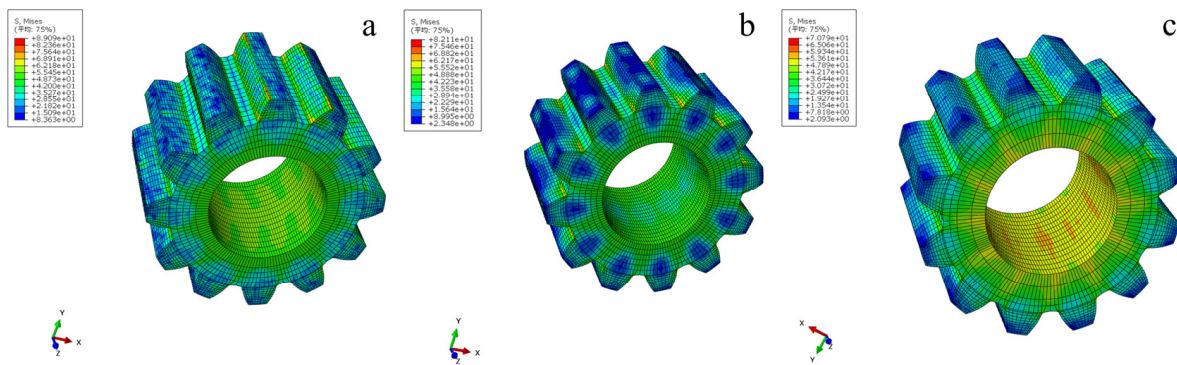


Figure 8. Stress contour maps before and after the modification of the element parameters.

In light of the findings delineated within Section 2, it was observed that the vibrational displacement of the external spline along the x direction exhibits a discernible periodic behavior. In order to efficaciously incorporate the displacement function to the external spline while simultaneously scrutinizing the ramifications of nonlinear vibration on the micro-motion-induced deterioration in spline couplings, the execution of Fourier transformation on the given periodic function is deemed indispensable. Consequently, upon applying the Fourier transformation, the derived vibrational displacement function corresponding to the external spline in the x direction can be articulated as follows:

$$\begin{aligned}
 f(x) = & a_0 + a_1\cos(\omega x) + b_1\sin(\omega x) + a_2\cos(2\omega x) + b_2\sin(2\omega x) \\
 & + a_3\cos(3\omega x) + b_3\sin(3\omega x) + a_4\cos(4\omega x) + b_4\sin(4\omega x) \\
 & + a_5\cos(5\omega x) + b_5\sin(5\omega x) + a_6\cos(6\omega x) + b_6\sin(6\omega x) \\
 & + a_7\cos(7\omega x) + b_7\sin(7\omega x) + a_8\cos(8\omega x) + b_8\sin(8\omega x)
 \end{aligned}$$

The values of $a_0 \sim a_8; b_0 \sim b_8; \omega$ under different working conditions are shown in Tables 4–7.

Table 4. The value of each parameter in the case of misalignment is not considered.

Parameter	Value	Parameter	Value
a_0	-1.752×10^{-13}	ω	73.3
a_1	-3.469×10^{-23}	b_1	4.988×10^{-23}
a_2	-2.858×10^{-17}	b_2	-2.52×10^{-17}
a_3	-7.569×10^{-23}	b_3	4.467×10^{-24}
a_4	3.69×10^{-21}	b_4	-9.637×10^{-22}
a_5	-7.706×10^{-23}	b_5	6.202×10^{-23}
a_6	-4.165×10^{-23}	b_6	-5.925×10^{-24}
a_7	-1.262×10^{-23}	b_7	-1.863×10^{-23}
a_8	-1.075×10^{-22}	b_8	-2.767×10^{-23}

Table 5. The value of each parameter in the case of $e = 0.1^\circ$.

Parameter	Value	Parameter	Value
a_0	5.948×10^{-5}	ω	73.3
a_1	4.517×10^{-22}	b_1	8.787×10^{-23}
a_2	-2.858×10^{-17}	b_2	-2.52×10^{-17}
a_3	1.854×10^{-21}	b_3	2.169×10^{-22}
a_4	1.611×10^{-18}	b_4	5.992×10^{-18}
a_5	1.982×10^{-22}	b_5	7.687×10^{-23}
a_6	2.35×10^{-21}	b_6	1.85×10^{-22}
a_7	8.903×10^{-22}	b_7	2.559×10^{-22}
a_8	1.809×10^{-21}	b_8	-1.32×10^{-22}

Table 6. The value of each parameter in the case of $e = 0.2^\circ$.

Parameter	Value	Parameter	Value
a_0	9.914×10^{-5}	ω	146.6
a_1	-2.858×10^{-17}	b_1	-2.52×10^{-17}
a_2	2.68×10^{-18}	b_2	9.988×10^{-18}
a_3	4.703×10^{-21}	b_3	1.938×10^{-22}
a_4	1.949×10^{-21}	b_4	1.391×10^{-21}
a_5	2.227×10^{-21}	b_5	2.22×10^{-22}
a_6	-2.466×10^{-22}	b_6	-4.824×10^{-22}
a_7	-1.207×10^{-20}	b_7	1.25×10^{-20}
a_8	4.952×10^{-21}	b_8	-1.306×10^{-21}

Table 7. The value of each parameter in the case of $e = 0.3^\circ$.

Parameter	Value	Parameter	Value
a_0	0.0001377	ω	1759
a_1	6.458×10^{-10}	b_1	-4.627×10^{-7}
a_2	1.487×10^{-8}	b_2	-6.889×10^{-11}
a_3	-3.309×10^{-12}	b_3	-1.587×10^{-9}
a_4	-1.307×10^{-10}	b_4	-1.671×10^{-12}
a_5	-2.029×10^{-12}	b_5	-6.603×10^{-11}
a_6	1.336×10^{-12}	b_6	1.336×10^{-12}
a_7	2.739×10^{-12}	b_7	6.573×10^{-11}
a_8	4.67×10^{-11}	b_8	-3.925×10^{-12}

5.2. Finite Element Analysis of Involute Spline Pairs of an Aero-Engine

5.2.1. Vibration Displacement of $f(e = 0^\circ)$ Fretting Damage Results

In an attempt to rationalize the mechanism underpinning the influence of vibration on the fretting damage instigated in involute spline pairs employing a vibration displacement of $f(e = 0.1^\circ)$, the fretting damage dataset corresponding to the external spline tooth surface was extracted from the simulation outcomes spanning a temporal interval of 0 to 0.1 s. Wear depth distribution curves over consecutive temporal fractions (0 to 0.1 s, divided into five distinct intervals) were thereby ascertained across both the axial and radial positions of the referenced external spline. Subsequently, differential curves that signify the temporal progression of wear depth for each tooth, both in the presence and absence of vibration displacement, were conceived. More specifically, the specified time duration of 0 to 0.1 s was partitioned into 20 intervals, and the mean wear depth corresponding to each such interval was computed. The aforementioned datasets, in turn, are presented graphically in Figures 9 and 10.

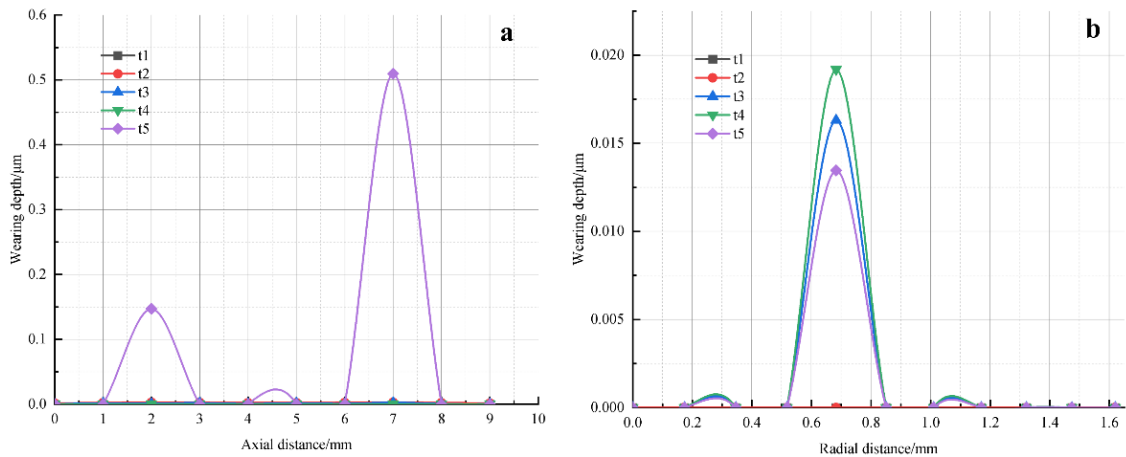


Figure 9. Wear Distribution Chart of an External Spline Single Tooth Subject to a Vibration Displacement of $f(e = 0^\circ)$: (a) along axial direction; (b) along radial direction.

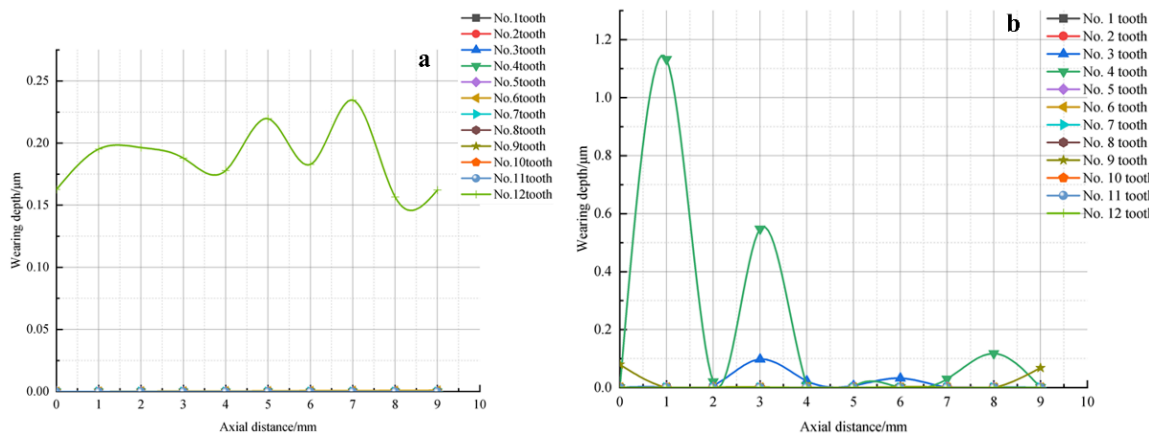


Figure 10. Wear Distribution Charts of External Spline Tooth Surfaces with and without Vibration (Vibration Displacement of $f(e = 0^\circ)$): (a) without vibration of the external spline; (b) under external spline vibration.

As represented in Figure 9a, the external spline tooth surface manifests an insubstantial wear from time interval t1 to t4. However, during the period of t5, an acute increase in wear depth becomes noticeable, with the apogee of wear depth detected at the axial position of 7 mm. It is crucial to note that the nadir wear depths were recorded at axial positions located between 3–4 mm, 5–6 mm, and 8–9 mm. In Figure 9b, imperceptible wear during the period from t1 to t2 is indicated, while a gradual crescendo in the wear depth of both the internal and external spline tooth surfaces can be identified from the time interval t3 to t4. Encapsulated within the radial position of 0.5–0.85 mm, this wear is predominant. Nevertheless, during the time period t5, the wear depth registers a gradual descent. Examining Figure 10a, within the period of 0 to 0.1 s, insignificant overall wear is perceivable on teeth numbered 1 to 12 of the external spline in the absence of any vibration. There is a slightly exacerbated wear on tooth 12, the zenith of which is observed at the axial position of 7 mm. The remaining teeth display negligible wear. This dearth of wear could be related to the subtle wear on tooth 12, which may be attributed to considerations regarding mass eccentricity. Further elucidated in Figure 10b, in the presence of vibrational forces acting on the external spline, the quantity of teeth demonstrating wear amplifies. The wear depth is the most pronounced for the fourth tooth at the axial position of 1 mm. The third tooth follows the fourth in wear, with a slight wear setting in and the peak wear depth recorded at the axial position of 3 mm. Other teeth predominantly demonstrate an insignificant degree of wear.

5.2.2. Vibration Displacement of $f(e = 0.1^\circ)$ Fretting Damage Results

In an effort to scrutinize the repercussions of vibrations on fretting degradation in involute spline couplings, with a vibrational displacement denoted by $f(e = 0.1^\circ)$, external spline tooth surface fretting deterioration information was gleaned from the simulation outcomes. This dataset enables a comprehensive assessment of wear depth distribution profiles across distinct temporal milestones, encompassing both axial and radial positions of the external spline. In addition, temporally evolving, graphical representations delineating the wear depth for each tooth, encompassing scenarios with and without vibrational displacement, are shown in Figures 11 and 12. These illustrative curves serve to elucidate the dynamic interplay of wear depth evolution as a function of the vibrational phenomena.

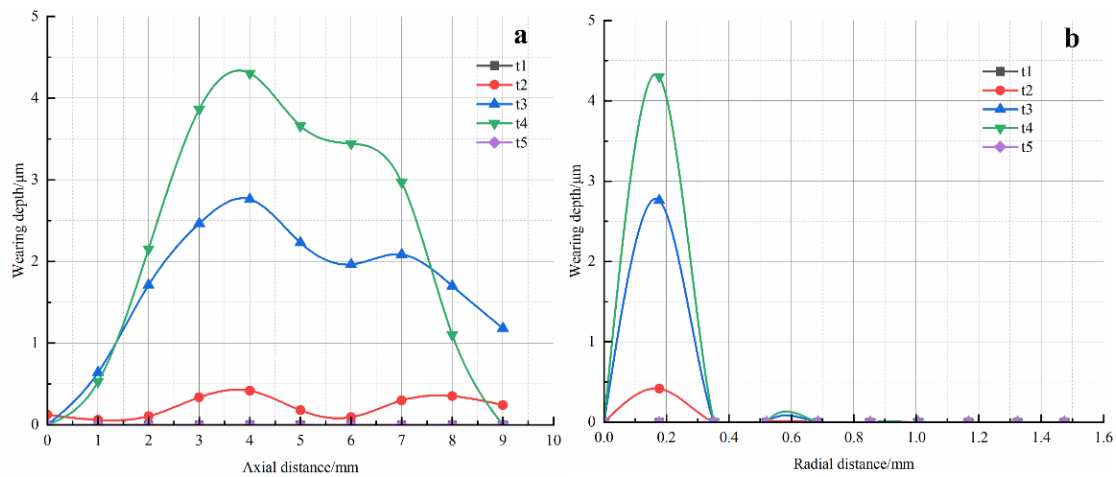


Figure 11. Wear Distribution Chart of an External Spline Single Tooth Subject to a Vibration Displacement of $f(e = 0.1^\circ)$: (a) along axial direction; (b) along radial direction.

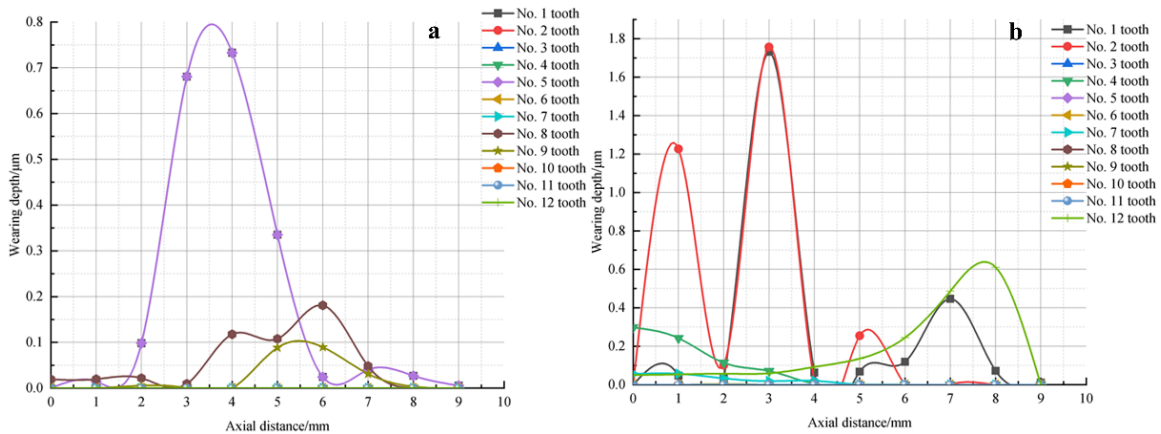


Figure 12. Wear Distribution Charts of External Spline Tooth Surfaces with and without Vibration (Vibration Displacement of $f(e = 0.1^\circ)$): (a) without vibration of the external spline; (b) under external spline vibration.

As delineated in Figure 11a, during temporal intervals t1 to t2 and t6, the wear depth along the external spline tooth surface is observed to be relatively homogenous and minimal, fluctuating within the 0 to 1 μm range. Conversely, during time intervals t3 to t4, a progressive escalation in the wear depth is witnessed on both internal and external spline tooth surfaces. The apogee of wear depth is discerned at the axial position measuring 4 mm. Conversely, nominal wear depths are discerned at axial positions of 0 mm and 9 mm. Figure 11b demonstrates marginal wear primarily during periods t1 and t6, with escalating wear depth from t2 to t5 on the spline tooth surface. This wear is primarily

concentrated in the radial range of 0 to 0.4 mm. Furthermore, at temporal sequence t_5 , the wear depth approximates to zero. This pattern can be attributed to the gradual reduction of contact stress to null, coupled with the lack of relative sliding motion between the contact surfaces of the spline couplings. A comparison of Figure 12a with Figure 11a reveals that incidences of angular misalignment engender a greater number of teeth afflicted with wear. Specifically, wear is most pronounced on the fifth tooth, evidenced by the maximum wear depth at an axial alignment of 3.5 mm. Teeth numbered 8 and 9 depict restrained wear, with the maximum wear depths at axial coordinates of 6 mm and 5.5 mm, respectively. The residual teeth do not display perceptible wear across numerous steps. Upon thorough analysis of Figure 12b, the collective impacts of misalignment and vibration are seen to contribute to augmented wear on multiple teeth. Specifically, the most severe wear is seen on the first and second teeth, with the pinnacle of wear depth observed at an axial location of 3 mm. Teeth designated as 4, 7, and 12 exhibit restrained wear, whilst the other teeth do not manifest any noticeable wear across various stages.

5.2.3. Vibration Displacement of $f(e = 0.2^\circ)$ Fretting Damage Results

In pursuit of deciphering the causal mechanism through which vibrations induce fretting damage in involute spline pairs operating under a vibration displacement of $f(e = 0.2^\circ)$, we extrapolated wear depth data encapsulated within the simulation outcomes pertaining to the external spline tooth surface. This assemblage of data bestows upon us the capability to generate distribution curves that illuminate the degree of wear depth at temporally varied junctures for both the axial and radial determinants on the external spline. Under further observation, Figures 13 and 14 provide visual representation of the wear depth delineation curves of each tooth, delineated within conditions both inclusive and exclusive of vibrational displacement, extrapolated over a sequential timeline. These illustrative curves grant valuable subtext pertaining to the dynamic shifts in wear depth comportment and extend an augmentative advantage towards the comprehensive analysis of the influence exerted by vibrations on the manifestation and severity of fretting damage.

As illustrated in Figure 13a, the wear between time intervals t_1 and t_5 is inconsequential, approaching a near-zero value. However, during the t_2 to t_4 period, the wear depth experiences a gradual escalation, with the maximum wear depth detected at axial positions of 2 mm, 4 mm, and 6 mm. Remarkably, during the t_3 to t_4 timeframe, the axial wear depth unveils periodic characteristics that progressively intensify over the course of elapsed time. Such periodicity is probably attributable to the oscillating nature of the vibration displacement throughout this specific duration. Figure 13b underscores that the wear depth during t_1 to t_4 remains nominal. Nonetheless, a sudden surge in wear depth is exhibited during t_5 , with the maximal value identifiable at the radial position of 1.2 mm. Contrasted with the axial orientation, the radial direction does not manifest periodic fluctuations in wear depth. Upon juxtaposing Figure 14a with Figure 11a, it can be inferred that an elevation in angle misalignment fails to engender wear in a larger number of teeth in the absence of vibration. However, the wear intensity undergoes an amplification. The fifth tooth witnesses the most pronounced wear, with the highest wear depth discernible at the axial position of 4 mm. Conversely, teeth numbered 1, 8, and 12 display comparatively moderate wear, with the peak wear degrees observed at axial locations of 2 mm and 4 mm. The residual teeth show minimal wear. In Figure 14b, when contrasted with Figure 12b, an enhanced angle misalignment under vibratory conditions does not culminate in an increased population of teeth undergoing wear, albeit, it substantially augments the wear intensity. Contrary to Figure 14a, the presence of vibration instigates an upsurge in both the quantity of teeth sustaining wear and the exacerbation of the wear degree. The third tooth is subjected to the most severe wear, with the maximal wear depth detected at the axial position of 4 mm. Teeth numbered 7, 8, 9, and 11 also endure significant wear at the 4 mm axial placement. In addition, teeth numbered 7, 8, 9, and 11 exhibit mild wear, while the remaining teeth present minimal wear.

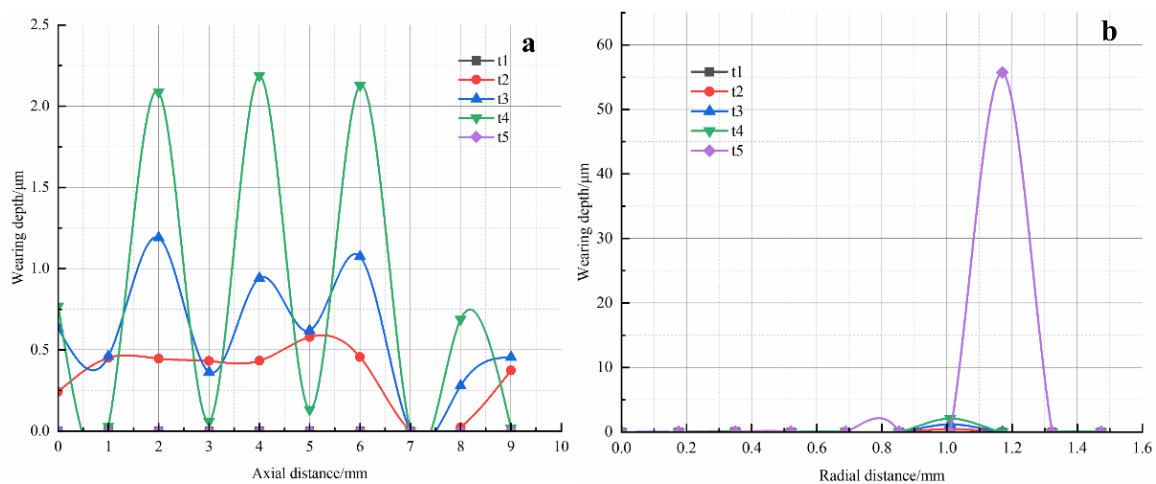


Figure 13. Wear Distribution Chart of an External Spline Single Tooth Subject to a Vibration Displacement of $f(e = 0.2^\circ)$: (a) along axial direction; (b) along radial direction.

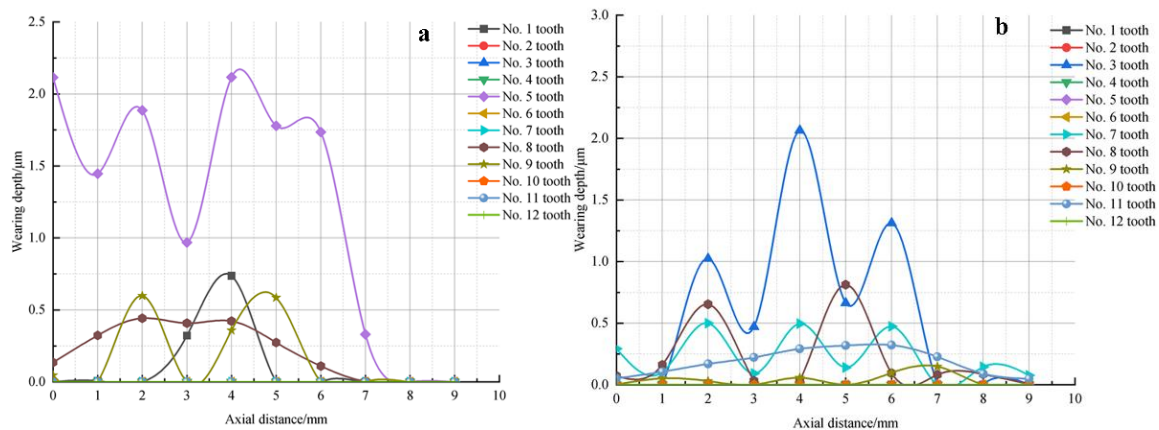


Figure 14. Wear Distribution Charts of External Spline Tooth Surfaces with and without Vibration (Vibration Displacement of $f(e = 0.2^\circ)$): (a) without vibration of the external spline; (b) under external spline vibration.

5.2.4. Vibration Displacement of $f(e = 0.3^\circ)$ Fretting Damage Results

To investigate the underlying mechanism governing the impact of vibration on fretting damage in involute spline pairs with a vibration displacement parameter $f(e = 0.3^\circ)$, we extracted wear depth data from the simulation outcomes pertaining to the external spline tooth surface. This data facilitated the acquisition of distribution curves delineating the wear depth at distinct temporal intervals for both axial and radial positions of the external spline. Moreover, Figures 15 and 16 exhibit wear depth progression curves for each tooth, encapsulating the comparison between scenarios with and without vibration displacement, contingent upon the time variable. These curves offer valuable insights into the dynamic evolution of wear depth, thereby enabling an in-depth analysis of vibration-induced fretting damage effects.

As illustrated in Figure 15a, during the initial phase t1, the wear is negligible and the axial wear depth distribution on the external spline tooth surface exhibits an unbroken smooth pattern. There is a steady escalation in wear depth from t2 to t3, culminating in maximum wear at an axial position of 2 mm. Conversely, a gradual decreasing trend in wear depth is seen from t4 to t5. Figure 15b further reveals a steady incremental pattern in wear depth from t1 to t4, reaching its zenith at the radial position of 1.2 mm. However, a subsequent decrement in wear depth is observed during t5. Radial wear in the external spline only occurs within the bounds of 1 mm and 1.4 mm. Referring to Figure 16a, an increment in angle misalignment does not cause an increased number of teeth to undergo

wear without vibration. Nonetheless, it does exacerbate the degree of wear. Tooth number 5 shows the highest wear severity, with the largest wear depth located at an axial position of 2 mm. Furthermore, a significant wear pattern is evident at a 2 mm axial position in the cases of the second, eighth, and ninth teeth. Meanwhile, the wear severity experienced by the second, eighth, and ninth teeth is comparatively mild, with the maximum wear depths occurring at axial positions of 5 mm and 0 mm, respectively. The residual teeth show trivial wear. Finally, looking at Figure 16b, vibration incites augmentation in both the number of teeth experiencing wear and the wear degree. The most severe wear is witnessed in the second tooth, with maximum wear depth observed at an axial position of 5 mm. Teeth numbered 1, 5, 8, and 11 display minimal wear while almost no wear is detectable in the remaining teeth.

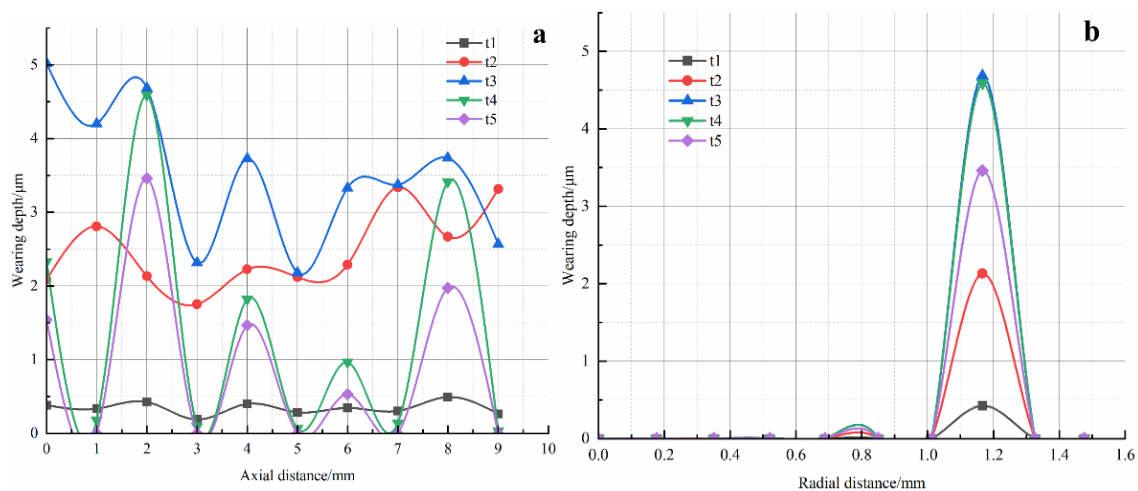


Figure 15. Wear Distribution Chart of an External Spline Single Tooth Subject to a Vibration Displacement of $f(e = 0.3^\circ)$: (a) along axial direction; (b) along radial direction.

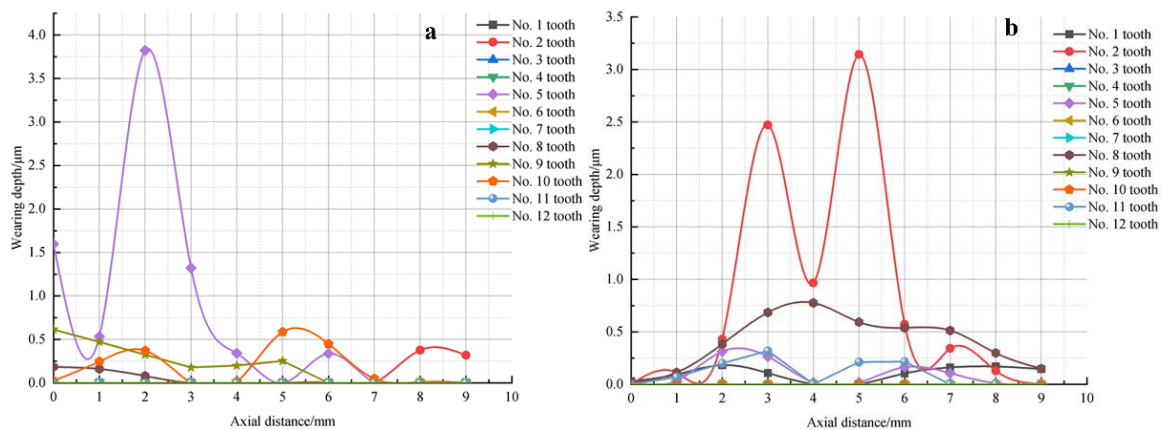


Figure 16. Wear Distribution Charts of External Spline Tooth Surfaces with and without Vibration (Vibration Displacement of $f(e = 0.3^\circ)$): (a) without vibration of the external spline; (b) under external spline vibration.

6. Experiment

6.1. Experimental Introduction

6.1.1. Experimental Device and Principle

The investigation of vibration and fretting damage in involute spline pairs within aero-engine systems was facilitated by a comprehensive experimental platform. This platform was primarily composed of three fundamental components, including a power output

system, a dedicated spline-couplings working platform, and a load application device. These essential components are meticulously depicted in Figures 17 and 18.

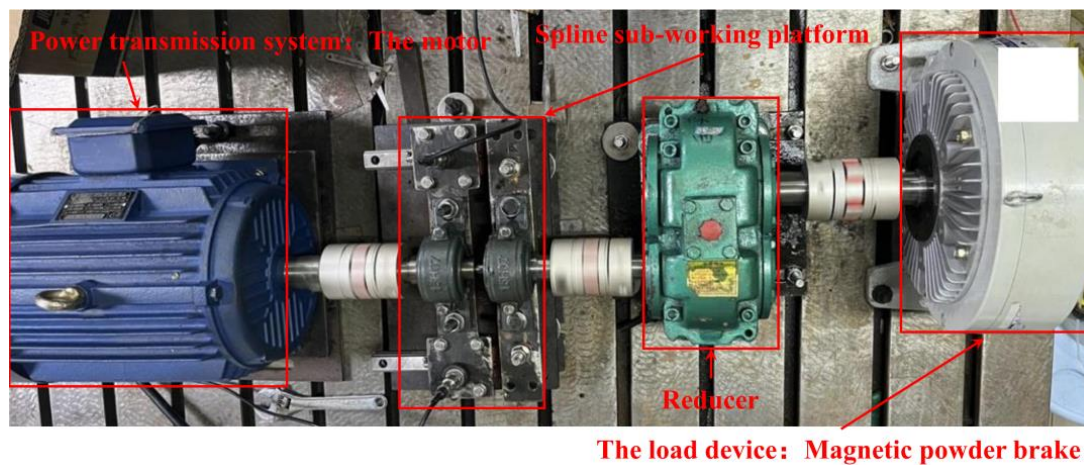


Figure 17. Experimental platform for vibration-fretting damage of involute spline pairs of an aero-engine.

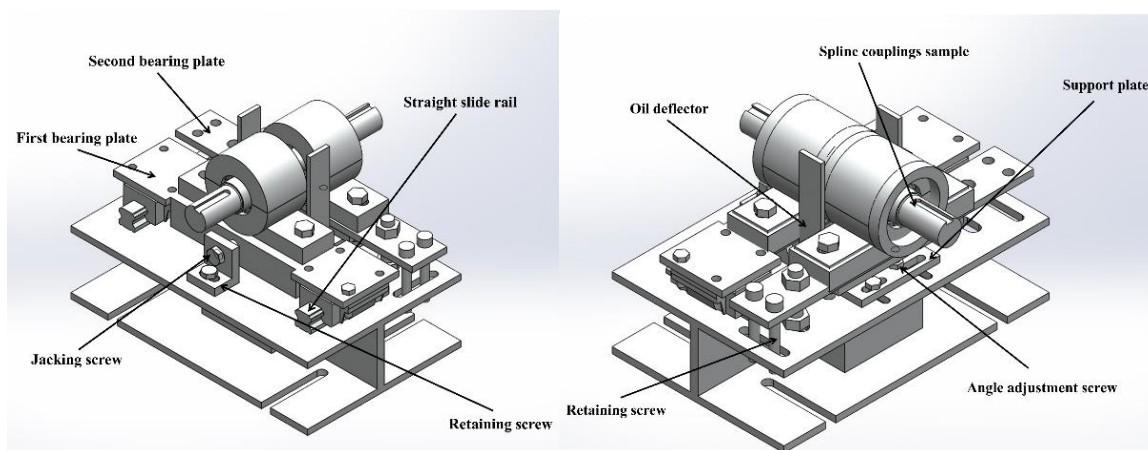


Figure 18. Structural schematic diagram of involute spline pairs of an aero-engine working platform.

As delineated in Figure 18, the support plate plays a crucial bifunctional role. In addition to its primary function of providing structural support, it also accommodates the provision for angle misalignment adjustments. Such modifications are facilitated via the incorporation of angle misalignment adjustment screws present on the support plate. Upon the insertion of the angle adjustment screw, a consequential tilting motion ensues in the external spline and its corresponding bearing seat in the axis direction. This deliberate maneuver engenders the required misalignment in the involute spline pairs associated with the aero-engine. Consequently, it ensures that the auxiliary angle is not confined to a centrally aligned position, thereby achieving optimal functionality.

6.1.2. Parameters of Test Piece

The objective of this experiment was to systematically examine the multifarious factors influencing fretting damage in involute spline pairs within aero-engine systems. The materials selected for this experimental platform were chosen for their prevalent application in aviation transmission systems. Comprehensive specifications of these materials are referenced in Figure 19, whereas essential material parameters are delineated in Table 8. The Vickers hardness values reported represent the average, derived from 15 distinct measurements conducted on the spline surface utilizing a Vickers hardness tester. Spline couplings were configured with an H6/h6 level of fit, incorporating an engaging part

diameter of 25 mm. To ensure optimal alignment, the spline shaft was strategically situated proximal to the motor shaft endpoint.

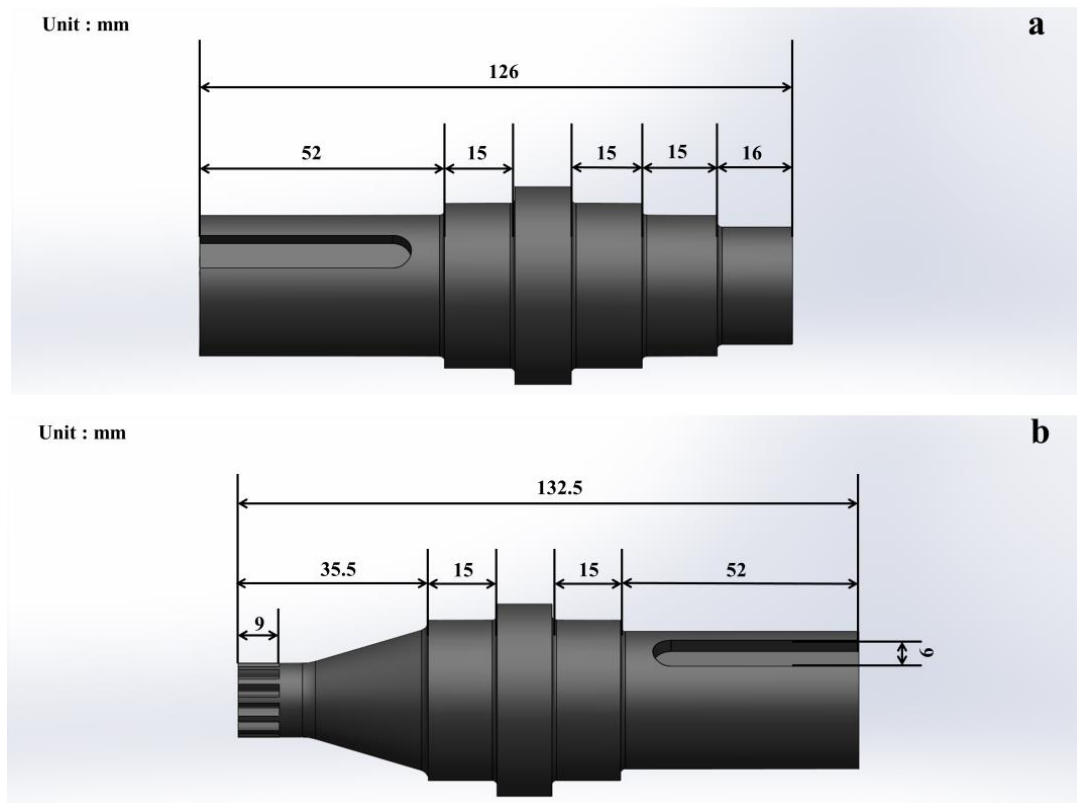


Figure 19. Diagram of basic parameters of involute spline pairs of an aero-engine: (a) internal spline; (b) external spline.

Table 8. Basic material parameters.

Material Name/Material Parameter	9310	32Cr3MoVA
Strength of extension σ_b /Mpa	≥ 1060	≥ 1080
Yield strength σ_s /Mpa	≥ 830	≥ 880
Extend rate δ /%	≥ 11	≥ 12
Shrinkage rate φ /%	≥ 50	≥ 40
Heat treatment	Hardening; Oil cooling; Tempering; Water cooling; Air cooling	Hardening; Oil cooling; Air cooling; Tempering; Air cooling; Tempering resistance; Argon shield
Average Vickers hardness after carbonization HV/V	529.21	521.25

6.1.3. Experimental Scheme

The experimental spline couplings were meticulously mounted on the designated platform, with the motor and brake collectively maintaining stable speed and load conditions. This experimental setup facilitated the emulation of authentic working conditions, encompassing spline shaft axis misalignment and deflection misalignment scenarios. Following an uninterrupted operational period on the platform, the experimental apparatus was disassembled for subsequent analysis. Scrutiny of wear patterns on the spline secondary tooth surface was executed utilizing scanning electron microscopy (SEM) and an Olympus DSX510 digital microscope. The investigation incorporated three distinct sets of fretting damage experiments, executed under varying working conditions, as delineated in Table 9. Given the inherent difficulties in ensuring precise control over spline angle misalignment, the present study primarily focused on angle misalignments of $e = 0^\circ$, $e = 0.1^\circ$, and $e = 0.2^\circ$.

Table 9. Experimental working conditions.

Experiment Group Number	Internal Spline Material	External Spline Material	Angle Misalignment	Lubrication	Induration	Rotate Speed
1	9310	32Cr3MoVA	0	Grease lubrication	All hardened (Carbonized)	1400
2	9310	32Cr3MoVA	0.1	Grease lubrication	All hardened (Carbonized)	1400
2	9310	32Cr3MoVA	0.2	Grease lubrication	All hardened (Carbonized)	1400

The experimental segment of this research entailed the execution of fretting damage investigations on spline couplings, in adherence with the conditions stipulated in the associated table. Throughout the experimental process, there was continual real-time monitoring of crucial parameters such as torque, rotational speed values, and the critical temperature at which damage transpired on the spline shaft. The overarching objective of these diverse explorations was to elucidate the effects of varying degrees of perpendicular or right-angle misalignment on the nonlinear vibrations and consequent fretting damage in involute spline pairs used in aero-engine systems. Such close observation and meticulous data collection are crucial in understanding the robustness and resilience of these ubiquitous and vital aircraft engine components.

6.2. Experimental Procedure

The experimental components were meticulously positioned on the designated experimental platform, ensuring an exact concentric alignment of the axes for each section of the platform prior to each investigation. In a bid to preserve experimental precision, a pair of bearings were affixed to each spline shaft; these did not necessitate removal after each individual experiment. The specific experimental protocols are delineated as follows:

- (1) Spline coupling specimens were positioned onto the two bearings of the working condition simulator. The placement secured the joint components of the two splines equidistantly nestled between the bearings.
- (2) The spline angles were adjusted to match the desired bearing displacement; concurrently, the lubrication condition of the spline shaft components was adjusted. This regulated condition emulation accurately replicated the operational circumstances of the spline couplings.
- (3) The loading apparatus was configured to the desired load capacity. Thus, the reducer's deceleration ratio was modulated, and the driving device's torque was set, achieving the necessary torque for effective spline coupling operation.
- (4) Upon attainment of the desired operational duration for the spline couplings, the experimental platform was powered down, and the specimens were carefully extracted for subsequent processing and treatment. The intricacies of tooth surface morphology were examined using 3D scanning electron microscopy (SEM) to explore the mechanisms underlying fretting damage. Simultaneously, an Olympus DSX510 digital microscope was deployed to observe the global fretting damage of the spline tooth surface across varied control groups. This process enabled the acquisition of fretting damage distribution data at different locations on the spline secondary tooth surface. This detailed analysis yielded a comprehensive comprehension of the fretting damage distribution across the entirety of the spline secondary tooth surface.

6.3. Experimental Result

6.3.1. The Fretting Damage Results of the External Spline Tooth Surface under All Neutral Conditions

Intensive scrutiny was executed on a prototypical instance of a worn tooth surface, as illustrated in Figure 20. This specific tooth surface manifested severe degradation, char-

acterized by the existence of numerous diminutive contours with a gentle sloping aspect. The formations of these topographical abnormalities were presumably precipitated by off-centered positioning and irregularly distributed forces during apparatus installation, which were not appropriately counterbalanced. The trio of distinct groups, representing varying types of worn tooth surfaces, displayed expansive zones of surface attrition. This was further punctuated by the inconspicuous presence of miniature pits within certain sectors. These pit formations remained relatively minute in scale. Absence of discernible micro-fissures reinforces the idea that any potential crack formations are likely to have undergone wear during their respective initiation and widening stages. Hence, fretting attrition is ascertained to be the principal failure mode for the exterior spline. This observation is congruent with the proposed predictive model for fretting-induced damage.

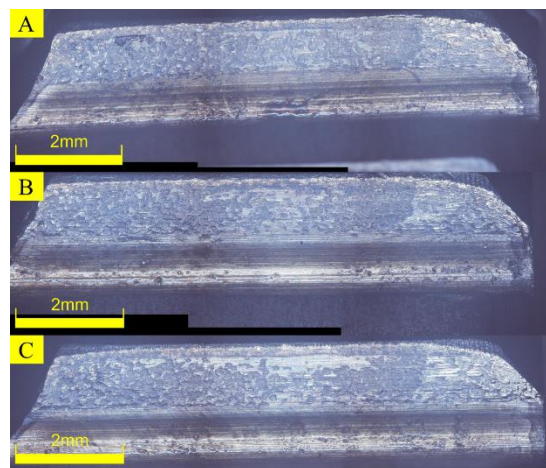


Figure 20. Electron microscopic image of fretting damage failure of external spline tooth surface with angle misalignment $e = 0^\circ$: SEM Images of Fretting Damage on Different Teeth of External Splines at $e = 0^\circ$ for (A–C).

As shown in Figure 21. In addition to the diminutive pit formations instigated by fretting wear, discernible regions of reddish hue within the pitted damage area are apparent. This coloration to red may be potentially ascribed to the inclusion of oxygen, while the irregular surface undulations could signify oxidative wear. The conspicuous presence of a plethora of wear marks further intimates incidents of abrasive wear. These pits, demonstrating a wide range of sizes, are constituted through a dynamic cycle of accumulation and evacuation of abrasive debris amid surface contacts during the wear process, suggestive of adhesive wear. Moreover, fatigue-induced fissures are apparent within these pits. A trend is noted where larger pits show a pronounced expansion of these cracks, while the smaller pits exhibit negligible propagation of fatigue cracks. Such disparity can be traced back to the relatively stunted dimension of these pits, leading to a nominally limited potential for crack propagation, insufficient energy to trigger internal crack expansion.

6.3.2. The Fretting Damage Failure Results of External Spline Tooth Surface under the Condition of Angle Misalignment $e = 0.1^\circ$

As shown in Figure 22. It is discernible that an augmentation in angular misalignment significantly exacerbated inflictions upon the external spline tooth surface. A substantial emergence of pits is evidenced, these often manifesting in a linear configuration—a characteristic attributable to the impact of angular misalignment fostering uneven load distribution on the tooth surface. High-load exposed areas exhibit higher pit densities. In parallel, there is noted an intensified ripple distribution, profoundly concaved valleys nestled between each ripple, and distinctly noticeable irregular wear markers. These concomitant effects can be traced to escalated angular misalignment, instigating amplified spline vibration and a heterogeneously distributed force on either end of the tooth surface, left and right.

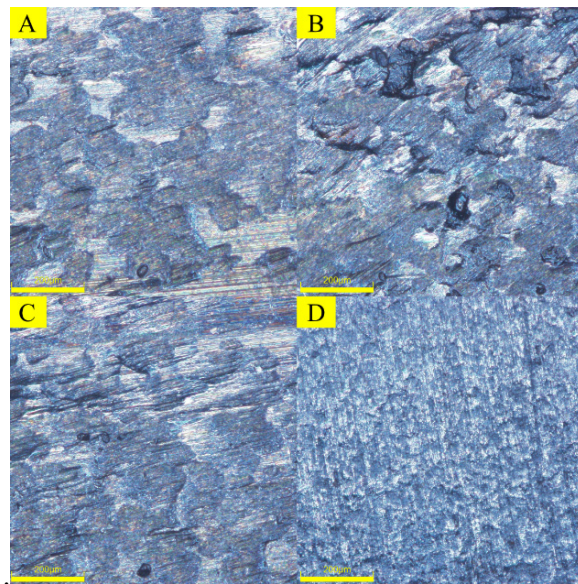


Figure 21. Surface morphology (SEM) of tooth surface of external spline with angular misalignment $e = 0^\circ$: SEM Images of Typical Damage Characteristics on Various Locations of External Spline Tooth Surfaces for (A–D) at $e = 0^\circ$.

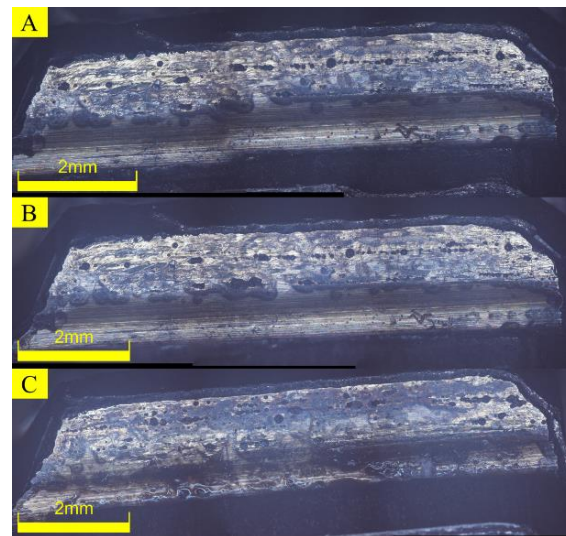


Figure 22. Electron microscopic image of fretting damage failure of external spline tooth surface with angle misalignment $e = 0.1^\circ$: SEM Images of Fretting Damage on Different Teeth of External Splines at $e = 0.1^\circ$ for (A–C).

As shown in Figure 23. Observation of the spline tooth surface reveals an abundance of silver stripes, an outcome of escalating friction along the tooth surface that promotes the production of grinding debris leading to surface scratches and extrusion of stratified scales owing to abrasive wear. Furthermore, pits of considerable size and dense distribution manifest themselves, with some of them coalescing to form larger cavities. Micro-cracks identified at the base of these pits engender their constant initiation and expansion, thus contributing to the pit enlargement and potential fatigue-induced degradation of the surface materials. The alignment of some pits in straight formations points towards adhesive wear instigated by grinding debris subjected to extrusion from the normal component of the meshing force. Adjacent to these pits, the visibility of reddish-brown deposits underscores the introduction of oxygen in the wear process, suggesting a scenario of oxidative wear.

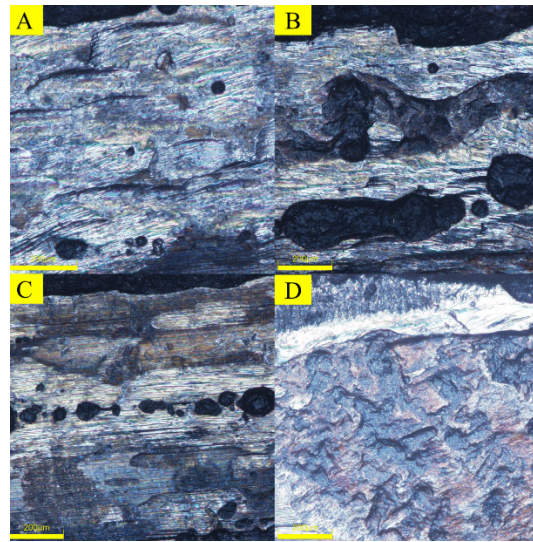


Figure 23. Surface morphology (SEM) of tooth surface of external spline with angular misalignment $e = 0.1^\circ$: SEM Images of Typical Damage Characteristics on Various Locations of External Spline Tooth Surfaces for (A–D) at $e = 0.1^\circ$.

6.3.3. The Fretting Damage Failure Results of External Spline Tooth Surface under the Condition of Angle Misalignment $e = 0.2^\circ$

As shown in Figure 24. From the perspective of a scientific research article, the following passage has been refined to enhance its professionalism: Observation demonstrates that an amplification in angular misalignment yields more pronounced deterioration on the tooth surface of external splines. Moreover, numerous small and subtly sloping formations are present on the tooth surface. This phenomenon might be attributed to the axial misalignment occurring in the right section of the splines during the installation process, thereby generating uneven forces borne by the left spline section as a consequence of incomplete engagement. The damage on the tooth surface of sections a, b, and c can be classified into two distinct regions. The right end presents more severe damage, characterized by a considerable expanse of irregular, diminutive faults. Conversely, on the left side, subtle sloping structures are evident, resulting from varying degrees of damage induced by misalignment.

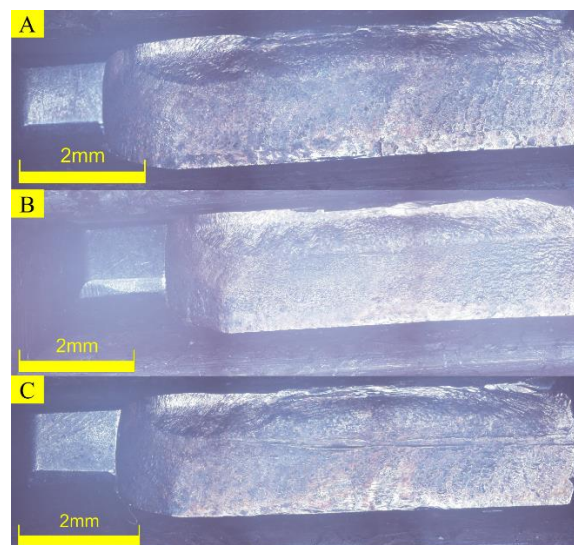


Figure 24. Electron microscopic image of fretting damage failure of external spline tooth surface with angle misalignment $e = 0.2^\circ$: SEM Images of Fretting Damage on Different Teeth of External Splines at $e = 0.2^\circ$ for (A–C).

As shown in Figure 25. Refined from the perspective of a scientific research article, the passage reads as follows: The tooth surface in contact with the spline exhibits numerous corrugated pits, densely dispersed and profound in depth. This effect is the result of exacerbated misalignment, which generates an increased level of wear debris between the contact surfaces of the spline under the normal component of the meshing force. In addition to this, oval grinding pits can be discerned, symptomatic of adhesive wear. Adjacent to these pits, a reddish-brown substance is produced as part of an oxidative reaction with air during friction and wear processes, suggestive evidence of oxidative wear. Moreover, a substantial crack is evident on the surface of the spline tooth, indicative of a larger-sized crater and elevated propensity for crack propagation inward, suggesting a considerable force behind the crack propagation.

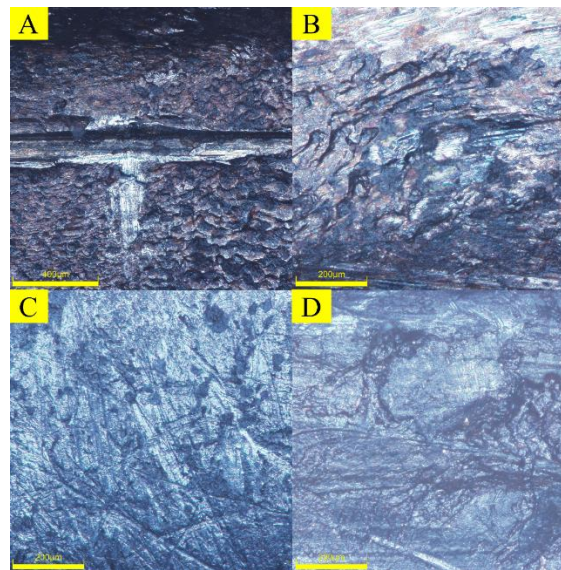


Figure 25. Surface morphology (SEM) of tooth surface of external spline with angular misalignment $e = 0.2^\circ$: SEM Images of Typical Damage Characteristics on Various Locations of External Spline Tooth Surfaces for (A–D) at $e = 0.2^\circ$.

In light of the analysis of nonlinear vibration results, finite element simulation outputs, and experimental observations, it becomes clear that an increase in angular misalignment contributes to a progressive enhancement in vibration mechanical characteristics (e.g., vibration displacement and normal meshing force) of the aerodynamic engine's involute spline pairs. As a result, the alternating stress experienced by the system's involute spline pairs intensifies, which translates to an exacerbated influence of nonlinear vibration on the system. This influence primarily materializes through the escalation of fretting damage observed on the secondary bonding teeth of the aerodynamic engine's involute spline pairs. The fretting damage failure mode predominantly encompasses a blend of fretting wear and fretting fatigue, particularly on the key teeth. Remarkably, in comparison to non-vibration conditions, the presence of vibration notably amplifies the wear severity on the secondary bonding teeth of the aerodynamic engine's involute spline pairs, manifested by a higher quantity of worn teeth. Thus, it can be concluded that nonlinear vibration aggravates the secondary fretting damage experienced by the aerodynamic engine's involute spline pairs. Furthermore, it is crucial to recognize that moderate angular misalignment compounds the severity of nonlinear vibration on the secondary system of the involute spline pairs, magnifying the fretting damage.

7. Conclusions

This manuscript endeavors to address the intricate resolution of the differential equations pertaining to involute spline pairs found in aerodynamic engines, entailing factors

such as misalignment, transverse vibration, and torsional vibration. The attained solution reveals the patterns of fluctuation in regards to vibration displacement and associated frequency. The derived vibration displacement function is subsequently incorporated into a meticulously construed finite element model of the involute spline pairs. This integration facilitates the emulation of the vibration behavior of these pairs, thus serving as a credible source of insight into the dynamics of their nonlinear interaction. A comprehensive assessment is conducted on the repercussion of vibration displacement under an array of angular misalignments, thereby elucidating the resultant fretting damage within the involute spline pairs operational within aerodynamic engines. This understanding contributes significantly to the empirical knowledge base that assists in the exploration of nonlinear vibration and fretting damage within other analogous coupling systems. It is noteworthy to emphasize that the primary focus of the incumbent research is solely to probe the influence of vibration displacement over the fretting damage in an aerodynamic engine's involute spline pairs. It is intended that future investigations extend towards exploring the influence exerted by other dynamic parameters of vibration on the fretting damage. In summation, the principal conclusions from the current exploration can be outlined as follows:

- (1) This study employs integrated preceding theories and computational methodologies to effectively resolve a MATLAB-anchored dynamic model pertaining to involute spline pairs in aerodynamic engines. The central area of scrutiny encompasses examination of the influences exerted by variations of angular misalignment on aspects such as vibration displacement, vibration frequency, and the normal forces acting on the meshing interfaces. Observations reveal that the vibration displacement demonstrates an escalation congruent with the augmentation of angular misalignment. Particularly evident is the appreciable increase in vibration displacement when the angular misalignment spans between 0° and 0.1° . Although this ascension persists, the incremental rate decelerates with a further increase in angular misalignment, notably from 0.1° to 0.3° . An eminent amplitude of displacement was observed around a frequency of 250 Hz, and this tended to intensify gradually, signaling a consequent elevation in the alternating stress pervading the system. This escalating stress further stimulates a progressive accrual in the damage induced by the nonlinear vibrations. Additionally, as the angular misalignment escalates, the normal meshing force imposed on each tooth surface exhibits a consistent magnification. Concurrently, the non-uniformity in the distribution of the normal meshing forces across the teeth surfaces exacerbates.
- (2) This study introduces an innovative approach to predicting fretting damage in the involute spline pairs of aerodynamic engines, with the stipulation that fretting wear serves as the primary failure mode. Optimization of the Archard model paves the way towards deriving a novel fretting wear prediction model. Vibration data harnessed from MATLAB was subjected to Fourier transformations, yielding a vibration function which was subsequently integrated into the boundary conditions of the definitive finite element model. The process of analysis and requisite computations were executed in the ABAQUS environment. Findings from the simulation affirm that, contrasted with conditions void of vibrations, the existence of vibrations culminates in a heightened incidence of wear in the external spline teeth. Additionally, certain key teeth experience an intensified degree of wear. A supplemental observation reveals that as the angular misalignment progressively escalates, the fretting wear on the spline teeth becomes dramatically pronounced.
- (3) Supplementary to the primary research, an experimental platform was specifically established to investigate the intricacies of fretting damage within the involute spline pairs of aerodynamic engines. A critical examination of the subsequent experimental results substantiated that the archetypal failure mode of fretting damage on the external spline tooth surface was predominantly characterized by fretting wear. Nonetheless, it is noteworthy to mention that fretting fatigue was continually observed in perpetuity throughout the entire fretting cycle. This concurrent presence suggested a competition and meaningful interplay with the defined fretting wear. In an attempt

to assiduously quantify the extent of fretting damage in the involute spline pairs of aerodynamic engines, the wear depth was employed as a reliable measure. Moreover, it was unequivocally established that the propensity and severity of fretting damage in these spline pairs escalated correlatively with angular misalignment under the influence of vibration conditions. This discernment not only sheds light on a key contributing factor but also serves to reinforce the credibility and accuracy of the preceding simulation results.

Author Contributions: Conceptualization, X.X. and Y.L.; methodology, X.X.; software, Y.L.; validation, Y.L., K.L. and L.S.; formal analysis, Y.J.; supervision, N.Z. All authors have read and agreed to the published version of the manuscript.

Funding: The authors acknowledge financial support from the National Natural Science Foundation (Grant No.52005312) and support from the Sichuan Science and Technology Program (2023YFG0201).

Data Availability Statement: Data are contained within the article.

Conflicts of Interest: Author Liqi Sui was employed by the company Yibin Fengchuan Powertrain Technology. The remaining authors declare that the research was conducted in the absence of any commercial or financial relationships that could be construed as a potential conflict of interest.

References

- Liu, Z. Bent-Torsional Coupling Vibration Characteristics of Rotor Bearing System. Ph.D Thesis, Chongqing University, Chongqing, China, 2016.
- Huang, Z.L.; Song, G.Q.; Zhang, Z.C. Dynamic Analysis of cutting head Rotor System of Roadheader under Two Loads. *J. Vib. Meas. Diagn.* **2020**, *40*, 941–947.
- Long, X.; Zhang, X.N.; Dong, C. Research on Abnormal wear of spline in Involute. *Archit. Eng. Technol. Des.* **2020**, *6*, 4161.
- Zeng, G.; Ma, C.J.; Pang, D.Q. Coupling Vibration Characteristics of High linear Speed rotor-Planetary Gear System in Mechatronic Composite Drive. *Acta Oramentologica Sin.* **2023**, *44*, 156–164.
- Du, W.L.; Li, W.; Jiang, Z. Analysis of flexural and torsional Coupling Vibration of permanent magnet Motor Rotor System of Shearer under Load Excitation. *J. Vib. Shock* **2023**, *42*, 237–244.
- Wang, P.F.; Yang, Y.; Xu, H.Y. Influence of Static and Dynamic misalignment of Rolling Bearing on Nonlinear Vibration Characteristics of rotating Subsystem. *J. Cent. South Univ.* **2019**, *30*, 871–903. [[CrossRef](#)]
- Wang, L.K.; Wang, A.L.; Yin, Y.J. Vibration characteristics of complex rotor of aeroengine considering support constraints. *J. Aerodyn.* **2023**, *38*, 901–912.
- Ge, W.W.; Sun, W.L.; Ma, Y.H. Dynamic Characteristics Analysis of Rotor-Bearing System for High Speed Permanent Magnet Motor. *Mach. Tool Hydraul.* **2021**, *49*, 169–172.
- Xiao, L.; Xu, Y.; Chen, Z.; Zhang, L. Non-linear dynamic response of misaligned spline coupling: Theoretical modeling and experimental investigation. *J. Vib. Control* **2022**, *29*, 1590–1605. [[CrossRef](#)]
- Cura, F.M.; Mura, A. Theoretical and numerical evaluation of tilting moment in crowned teeth splined couplings. *Meccanica* **2018**, *53*, 413–424. [[CrossRef](#)]
- Cura, F.M.; Mura, A. Analysis of a load application point in spline coupling teeth. *J. Zhejiang Univ. Sci.* **2014**, *15*, 02–308. [[CrossRef](#)]
- Curfi, F.; Mura, A.; Gravina, M. Load distribution in spline coupling teeth with parallel offset misalignment. *J. Mech. Eng. Sci.* **2012**, *227*, 2195–2205.
- Guo, Y.; Lambert, S.; Wallen, R.; Errichello, R.; Keller, J. Theoretical and experimental study on gear-coupling contact and loads considering misalignment, torque, and friction influences. *Mech. Mach. Theory* **2016**, *98*, 242–262. [[CrossRef](#)]
- Zhao, G.; Liu, Z.; Ye, J.; Chen, F. Study on Dynamic Characteristics of Rotor-Misaligned Spline Coupling System. *J. Vib. Shock* **2009**, *28*, 78–82.
- Zhao, G.; Liu, Z.S.; Ye, J.H.; Chen, F. Misaligned Meshing Force Model of Gear Coupling and Its Influence on Dynamic Characteristics of Rotating Subsystem. *J. Harbin Eng. Univ.* **2009**, *30*, 33–39.
- Zhao, G.; Guo, J.; Wang, X.; Wang, Y.L. Research on Bend-Torsional Coupling Vibration of Rotor-Gear Coupling System. *J. Aerosp. Power* **1999**, *109*, 61–65.
- He, C.; Gu, Y.; Yang, K. Characteristics of Bent-Torsional Coupling Vibration of Misaligned Rotor in Gear Coupling. *J. Mech. Strength* **2005**, *75*, 725–729.
- Fu, B.; Zhou, J.; Peng, B.; An, X. Characteristics of Misalignment flexural and torsional Coupling Vibration of Fixed Rigid Coupling. *J. Huazhong Univ. Sci. Technol. (Nat. Sci. Ed.)* **2007**, *34*, 96–99.

19. Jing, J.; Gao, T.; Chen, C. The study on spline coupling dynamic coefficients and its impact on rotor stability. In Proceedings of the ICSV2016-23rd International Congress on Sound and Vibration: From Ancient to Modern Acoustics, Shanghai, China, 10–14 July 2016; State Key Laboratory of Mechanical System and Vibration, Shanghai Jiao Tong University: Shanghai, China, 2016. From Ancient to Modern Acoustics.
20. Jing, J.P.; Gao, T.; Mei, Q. Stability Analysis of Spline Connected Rotor System. *Noise Vib. Control* **2016**, *36*, 40–45.
21. Yang, G.L.; Zhu, L.L.; Zhao, L.C. Axial System Angle Misalignment Analysis of Radial Vibration Characteristics. *Mach. Des. Manuf.* **2018**, *10*, 125–126.
22. Tuckmantel, F.W.D.S.; Cavalca, K.L. Vibration signatures of a rotor-coupling-bearing system under angular misalignment. *Mech. Mach. Theory* **2019**, *133*, 559–583. [[CrossRef](#)]
23. Zhang, X.; Su, X.; Lu, H. Analysis of dynamic characteristic for misalignment-spline gear shaft based on whole transfer matrix method. *J. Vibro Eng.* **2018**, *20*, 1392–1408.
24. Mura, A.; Francesca, C.; Molfetta, A.D. Investigation of bearings overloads due to misaligned spline shafts. *Procedia Struct. Integr.* **2018**, *5*, 52–57. [[CrossRef](#)]
25. Patil, S.B.; Patil, S.R. Experimental and numerical analysis of a load distribution along the length of contact in involute spline shaft. *Int. J. Adv. Technol. Eng. Explor.* **2019**, *6*, 30–44. [[CrossRef](#)]
26. Xue, X.; Wang, S.; Yuan, R. Nonlinear Dynamic Characteristics of Involute Spline Pair. *J. Harbin Inst. Technol.* **2015**, *47*, 107–111.
27. Xue, X.Z.; Wang, S.M. Dynamic Characteristics and Load Coefficient Analysis of Involute spline pairs. *Adv. Mater. Res.* **2014**, *890*, 450–454. [[CrossRef](#)]
28. Xue, X.Z.; Wang, S.M.; Yuan, R. *Investigation of Load Distribution among Teeth of an Aero-Engine Spline Coupling*; Springer: Berlin/Heidelberg, Germany, 2016; Volume 367, pp. 1155–1162.
29. Chen, Y.; Li, J. *Review on Bend-Torsional Coupled Vibration of Turbo-Generator Shafting*; Turbine Technology: Harbin, China, 2012; Volume 54, pp. 161–164.
30. Liu, Z.; Cui, Y.; Huang, W. Study on Nonlinear Dynamics Characteristics of Coupled Flexural and Torsional Vibration of Rotor. *China Mech. Eng.* **2003**, *5*, 69–71.
31. Zheng, W.; Wang, S.; Jie, X. Research on Fretting Wear Mechanism and Wear Prediction Method of Aircraft Involute Spline. Ph.D Thesis, Northwestern Polytechnical University, Xi'an, China, 2017.
32. Xue, X.; Huo, Q.; Liu, J. Nonlinear Vibration Characteristics of the Involute Spline Coupling in Aeroengine with the Parallel Misalignment. *Int. J. Aerosp. Eng.* **2021**, *2021*, 1–19. [[CrossRef](#)]
33. Xue, X.; Huo, Q.; Zheng, J.; Chen, X.; Qin, L. Research on anti-fretting wear of aviation involute spline pair based on tooth profile modification. *China Mech. Eng.* **2019**, *30*, 2447–2455.
34. Xue, X.Z.; Huo, Q.X.; Hong, L. Fretting wear-fatigue life prediction for aero-engine's involute spline pairs based on ABAQUS. *J. Aerosp. Eng.* **2019**, *32*, 1–9. [[CrossRef](#)]

Disclaimer/Publisher's Note: The statements, opinions and data contained in all publications are solely those of the individual author(s) and contributor(s) and not of MDPI and/or the editor(s). MDPI and/or the editor(s) disclaim responsibility for any injury to people or property resulting from any ideas, methods, instructions or products referred to in the content.